*remote sensing*

MDPI

*Article*

# Statistical Characteristics of Cloud Occurrence and Vertical Structure Observed by a Ground-Based Ka-Band Cloud Radar in South Korea

**Bo-Young Ye [1], Eunsil Jung [2], Seungsook Shin [3] and GyuWon Lee [1,*]**

[1] Department of Astronomy and Atmospheric Sciences, Center for Atmospheric REmote sensing (CARE), Kyungpook National University, Daegu 41566, Korea; boyoungye@knu.ac.kr
[2] Department of Advanced Science and Technology Convergence, Kyungpook National University, Sangju 37224, Korea; eunsil.jung@knu.ac.kr
[3] National Institute of Meteorological Sciences, Korea Meteorological Administration, Segwipo 63568, Korea; tmdtnr2@korea.kr
* Correspondence: gyuwon@knu.ac.kr; Tel.: +82-53-950-6361

Received: 21 June 2020; Accepted: 9 July 2020; Published: 13 July 2020


**Abstract:** The cloud measurements for two years from the vertical pointing Ka-band cloud radar at Boseong in Korea are used to analyze detailed cloud properties. The reflectivity of the cloud radar is calibrated with other vertical pointing radars compared with the two disdrometers. A simple threshold-based quality control method is applied to eliminate non-meteorological echoes (insects and noise) in conjunction with despeckling along the radial direction. Clouds are classified into five types: high (HC), middle (MC), low (LC) for non-precipitating clouds, and deep (RainDP) and shallow (RainSH) for precipitating clouds. The average cloud frequency was about 35.9% with the maximum frequency of 50% in June for the total two-year sampling period. The RainDP occurred most frequently (11.8%), followed by HC (9.3%), MC (7.4%), RainSH (4.4%), and LC (2.9%) out of the average occurrence of the total 35.9%. HC and RainDP were frequently observed in summer and autumn, while RainSH, LC, and MC were dominant in the winter due to the dominant cloud development by the air-sea interaction during the cold air outbreak. The HC showed a significant seasonal variation of the maximum height and the rapid growth in the layer above 7 km (about −15 °C) in summer and autumn. This rapid growth appears in HC, MC, LC, and RainDP and is linked with rapid increases in Doppler velocity and mass flux. Thus, this growth is originated from the dominant riming processes in addition to depositional growth and is supported by an updraft in the layer between 6 and 8 km. MC showed a single frequency peak around 6 km with rapid growth above and strong evaporation below. The Doppler velocity of MC rapidly increases above 8 km and is nearly constant below this height due to strong evaporation except in the summer. LC had a similar trend of reflectivity (rapid growth in the HC region and strong evaporation in the lower region) lacking high frequency in the MC region. Unlike LC, the RainDP had continuous growth toward the ground in the entire layer with rapid growth in the HC and MC regions. In addition, two modes (cloud and precipitation) appear on the ground in spring and fall with the vertical continuity of the high frequency in the precipitation mode. The precipitation growth was most efficient in RainSH in summer with a reflectivity gradient of about 20 dBZ $km^{-1}$ and frequent updrafts larger than 1 m $s^{-1}$ and was smaller in the MC and HC regions.

**Keywords:** cloud occurrence; vertical structure; cloud radar; cloud types; cloud and precipitation modes; updraft; riming process

## 1. Introduction

Clouds are critical in the climate by maintaining radiative balance through the emission, absorption, and scattering of solar radiation, and they are closely related to atmospheric circulation. Thus, an understanding of their horizontal distribution, vertical structure, and microphysical properties is essential to resolve the uncertainty in predicting the climate and its change. The cloud microphysical characteristics are critical in atmospheric radiation models due to their strong regional characteristics.

Various techniques are used to observe clouds and their characteristics with satellites, ceilometers, lidars, and cloud radars. The satellites usually detect clouds by the brightness temperature in the upper part of the atmosphere and are advantageous to observe the horizontal distribution of clouds. Although the satellites equipped with lidar or radar can observe the vertical structure of clouds and are suitable for analyzing global characteristics using long-term data, it is challenging to monitor a specific area continuously. However, the ceilometer, lidar, and cloud radar typically detect vertical profiles of clouds and, therefore, are advantageous for understanding the vertical structure of clouds with fine time and spatial resolution. The ground-based instruments using a laser (ceilometer and lidar) are useful for the detection of cloud base height but are limited to detect cloud top height due to severe attenuation by cloud and precipitation particles [1,2].

In contrast, a cloud radar using a microwave is less attenuated by cloud and precipitation than the optical instruments and can provide vertical cloud information. Furthermore, high-resolution data can be acquired in time and space. Although the cloud radar is limited in that it cannot observe synoptic phenomena due to vertical profiling at one point or limited horizontal coverages, the cloud radar can provide valuable insights into the dynamics of clouds through continuous observation over several years [3]. These long-term observations of vertical cloud profiles collected from cloud radars can be used to understand the statistical characteristics of different types of clouds.

To better use the observed cloud information, quality control of cloud radar data such as non-meteorological echoes, mitigation, and reflectivity (Z) calibration should be performed. The cloud radar has a small beamwidth, which has less influence of ground echoes received from sidelobes, but non-meteorological echoes from insects are a big issue. The insect echoes have higher reflectivity values due to a large backscattering cross-section even at its small number concentration. They are frequently observed at higher altitudes than the top of the convective boundary layer in the morning, making it challenging to distinguish between insects and low-level clouds [4,5]. They were removed by using parameters such as their altitude, average moving speed, linear depolarization ratio (LDR), and spectral characteristics [6–9].

Precipitation attenuation severely affects the cloud radar, limiting the maximum observed radar reflectivity in the statistical analysis. There is also an issue of the possible quantification of radar calibration that can be performed by comparing the observed drop size distribution (DSD) from nearby disdrometers or by using the self-consistency of dual-polarimetric variables [10]. Regular calibrations are needed using a disdrometer for each precipitation case to characterize clouds and validate the numerical modeling and climate model [11–13].

After the quality control, we can analyze cloud characteristics, such as seasonal characteristics, and annual and monthly variations from cloud observation data collected over a long period [1,14,15]. Kalesse and Kollias [16] compared the characteristics of the high cloud using the millimeter-wavelength cloud radar (MMCR) data observed at the Southern Great Plains (SGP) and the Manus of Atmospheric Radiation Measurement (ARM) program. Zhang and Chen [17] used the MMCR and radiosonde from the SGP site to classify the cloud types and analyze the seasonal variations of top height, base height, and thickness of the cloud. They showed that the high cloud was the most frequent during all seasons and the multi-layer cloud was the least frequent. Furthermore, studies on cloud dynamics and thermodynamics for each type of cloud, combining long-term cloud statistics and numerical model analysis, are actively being conducted. Kollias et al. [3] analyzed cloud characteristics by cloud types using the MMCR data for 6.5 years at the ARM SGP site. Cirrus was the most frequent type and seasonal variations of cloud base height were clearly observed. The analysis with the radiosonde

data and the European Centre for Medium-Range Weather Forecasts analysis field revealed that the single-layer continental status was associated with strong large scale forcing. Lamer et al. [18] analyzed the changes in the mass flux of the shallow cumulus with environmental humidity from two-year data in Barbados.

Cloud studies in South Korea have been based on surface cloud observation by human observers accumulated over several years [19,20]. Kim and Hong [19] analyzed the seasonal variation of cloud types, cloud height, and cloudiness using the surface cloud observation data from 10 locations on the Korean Peninsula for eight years from 1983 to 1990. Yeh et al. [20] reported relationships among cloud type, cloudiness, surface temperature, and rainfall amount in four major cities (Seoul, Gangneung, Gwangju, and Daegu) from 1976 to 1995. According to Yeh et al. [20], the stratocumulus was the most frequent regardless of the season (the same as Kim and Hong [19]) and the cirrocumulus was the least frequent. Regarding human observation, cloud information is easily determined by the subjective judgment of the observer. Recently, studies on cloud and precipitation were conducted using remote sensing equipment. Song and Sohn [21] investigated precipitation patterns in the Korean Peninsula using Tropical Rainfall Measuring Mission Precipitation Radar (TRMM PR) data for 10 years (2002 to 2011) and classified them as continental precipitation due to strong convection and oceanic precipitation by shallow clouds. Cho et al. [22] showed 63% of cloudy days in the Boseong site during the summer season (June to August) using cloud base height data from a ceilometer for two years (August 2013 to July 2015). Lee et al. [23] analyzed clouds occurring in Seoul from January 2014 to December 2016 using two ceilometer data. They found that the average cloud occurrence rate in Seoul is 54.3%, and the cloud frequency is 70% to 77% in the summer season. They also analyzed the vertical characteristics of cloud occurrence and revealed that the peak of cloud base height with 16% to 23% was represented mostly between 1000 and 1500 m for the entire period.

Currently, cloud studies are being performed using the Ka-band cloud radar installed at Boseong, Korea. Oh et al. [24] compared the cloud top height of the cloud radar with that of Communication, Ocean and Meteorological Satellite (COMS). According to Oh et al. [24], the average top height observed by the cloud radar was lower than that estimated by COMS, and this difference tended to be larger with increasing rainfall intensity. Furthermore, the cloud radar can effectively detect the cloud top height that occurred within 300–15,000 m during no rain events. Ye et al. [25] showed that the low cloud (including the precipitation cloud) was most frequently observed from September to October 2013 using the cloud radar. Oh et al. [26] also obtained the result that low cloud is most frequent by comparing the top and base height of the cloud between the cloud radar, ceilometer, and COMS data. However, these studies are limited to less statistical characteristics of clouds with the limited data set. Furthermore, no study exists on the vertical structure of clouds and seasonal statistical analysis according to cloud types. Therefore, this study aims to analyze the seasonal and vertical characteristics of the cloud measured by the cloud radar at the Boseong site. The purpose of this study is to provide properties of cloud occurrence and the vertical structure of different cloud types from the cloud radar data.

In this study, the cloud radar reflectivities were calibrated by comparing the vertically pointing X-band radar (VertiX) and micro rain radar (MRR) that are calibrated by the observed DSD from two disdrometers for rain events. We also removed the non-meteorological echoes caused by insects and other targets using the characteristics of radar parameters. After applying the quality control, the cloud types were determined by using their height from the reflectivity data collected over two years. The cloud occurrence and vertical structure of reflectivity and the Doppler velocity ($V_D$) were analyzed according to cloud types and seasons.

## 2. Data

The cloud radar installed in the Boseong Standard Weather Observatory (BSWO, Figure 1) since 2013. The BSWO is operated as a supersite where various instruments are installed to monitor weather systems approaching from the southern oceans. The BSWO has 3.4 days of freezing a year (the number

of days with the daily maximum temperature less than 0 °C per year), an average annual temperature of 13.2 °C, and a total annual precipitation of 1595 mm (869 mm for June to August) [27].

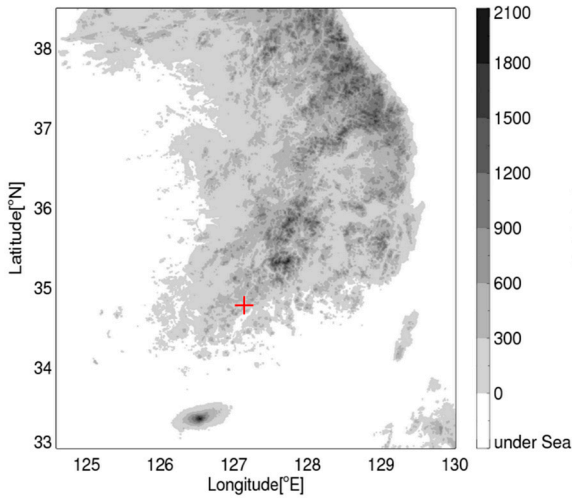


**Figure 1.** Location of the Boseong Standard Weather Observatory (BSWO) site (red cross), Deungryang-myeon, Boseong-gun in which the cloud radar is installed.

The cloud radar with a frequency of 33.44 GHz radiates horizontal polarized electromagnetic waves and receives the returned signal in the horizontal and vertical polarization. Thus, it observes only a dual-polarization variable, (LDR, dB), and other single-polarization variables. Detailed specifications are shown in Table 1. The sensitivity of radar reflectivity is about −30 dBZ at 5 km and the measurement uncertainty of the reflectivity is as low as 0.28 dB [25].

**Table 1.** Specifications of the Ka-band cloud radar manufactured by Beijing Santel Technology & Trading Corperation, China.

| | Parameters | Values |
|---|---|---|
| Transmitter | Type | Magnetron |
| | Peak power | ≥15 kW |
| | Frequency | 33.44 GHz |
| | Pulse width | 200 ns |
| | Pulse repetition frequency | 3.3 kHz |
| Antenna | Type | Parabola |
| | Diameter | 1.5 m |
| | Beamwidth | 0.42° |
| Scanning strategy | Number of gates | 1000 |
| | Sampling number | 126, 256 |
| | Gate spacing | 15 m |
| | Maximum observational range | 15 km |
| | Scan mode | Plan position indicator (PPI), Vertical pointing (VP) |
| | Time resolution (real elapsed time of PPI, VP) | 1 min (30 s, 45 s) |
| | Polarization mode | Single transmitting dual receiving |

The calibration of the cloud radar is critical for the quantitative use of the data but difficult due to its sensitivity and attenuation by precipitation. As typically performed for the weather radar, the cloud radar measured reflectivity can be directly compared with the reflectivity calculated from the disdrometers [10,28]. However, the disdrometer battles to measure smaller sized drops, leading to

a high uncertainty in low rainfall intensity and reflectivity [29–32]. Although the disdrometers had a better performance in moderate and heavy rain, the cloud radar had strong attenuation by rain as well as the Mie scattering effect. Thus, the direct comparison of the cloud radar and disdrometer did not provide proper unbiased results in different ranges of reflectivity, and we applied a two-step calibration into the cloud radar. First, the vertically pointing radars (VertiX and MRR) were calibrated with the disdrometers during the moderate rain period. The weaker echoes from the vertically pointing radar and cloud radar were compared to avoid possible attenuation in the cloud radar. Furthermore, the sensitivity of the VertiX is much higher than the MRR and strong cumulus is often observed in the VertiX. Thus, the comparison of the VertiX and cloud radar is possible in much lower values of reflectivity than that of the MRR and cloud radar. We derived the calibration bias of the cloud radar with the limited data set of the VertiX and compared it with the one derived from the comparison of the MRR and cloud radar to demonstrate the possibility of using different calibration pairs.

The reflectivity from the cloud radar was directly compared with that from the VertiX and MRR that were calibrated with the two ground-based disdrometers (two-dimensional video disdrometer, 2DVD, and particle size and velocity, PARSIVEL). The 2DVD has a two-dimensional optical system with a sampling area of 100 × 100 mm, a horizontal size resolution of 0.18 mm, and a vertical size resolution of 0.2 mm [33]. The size, shape, and velocity of the particles passing through the sampling area are observed by using two cameras that are aligned with two light sources at different heights. The PARSIVEL uses laser beams to measure the intensity of light and its occlusion time. These measurements are then converted into the size and fall speed of the hydrometeor. The PARSIVEL has a measuring area of 54 $cm^2$, a diameter range of 0.2–25 mm, and a velocity range of 0.2–20 $ms^{-1}$ with 32 velocity bins.

The VertiX uses a magnetron transmitter with a maximum peak power of 23 kW with a wavelength of 3.2 cm. The diameter of the antenna is approximately 1.2 m with a 1.8° of 3 dB beamwidth. The reflectivity, radial velocity, and power spectrum are calculated every 2 s with a vertical resolution of 45 m. The MRR observes the reflectivity, radial velocity, and power spectrum in the vertical incidence with a frequency-modulated continuous-wave (FM-CW) at 24 GHz (K-band, 1.25 cm wavelength). It has an antenna diameter of 0.6 m, a beamwidth of 2°, a time resolution of 10 s, and a vertical resolution of 200 m.

Quantifying of calibration bias was performed using the observed 36 rainfall events shown in Table 2. The pairs of 2DVD and VertiX (2–V) were available only for eight events and those of PARSIVEL and MRR (P–M) were available for all 36 events. The reflectivities from the 2DVD and PARSIVEL are unbiased and either the 2DVD or PARSIVEL can be first used to calibrate the VertiX or MRR. For simplicity, we used the 2–V pair only when this pair was available, otherwise, the P–M pair was used.

The cloud characteristics were analyzed from June 2014 to May 2016 for 2 years (the total days of available data are 504 days). Figure 2 shows the monthly percentage of available data and monthly cloud occurrence. The number of available data was derived from the threshold of burst power and was smaller than the actual cloud radar operation rate. During the period, the cloud radar operated and provided data of an average of 58%, with a maximum of 87% and a minimum of 14% (Figure 2). June, July, and August had a high availability of 78%, and November, December, January, February, and March had a low availability due to the radar hardware failures. The cloud occurrence was derived from only the available data. These statistics showed the poor representativeness of the cloud characteristics for May, November, and December.

**Table 2.** 36 rain events used to derive the calibration biases of the cloud radar reflectivity. The P–M and 2–V indicate the pairs of the particle size and velocity (PARSIVEL) and the micro rain radar (MRR), and the two-dimensional video disdrometer (2DVD) and the vertically pointing X-band radar (VertiX), respectively.

| No. | Periods (UTC) | Instrument | No. | Periods (UTC) | Instrument |
|---|---|---|---|---|---|
| 1 | 1800–2359 16 June 2014 | P-M | 19 | 0000–1559 20 Aug. 2014 | P-M |
| 2 | 0000–0459 17 June 2014 | P-M | 20 | 1900–2359 27 Aug. 2014 | P-M |
| 3 | 0400–1459 21 June 2014 | P-M | 21 | 0000–0759 28 Aug. 2014 | P-M |
| 4 | 0000–1559 2 July 2014 | 2-V | 22 | 0400–2259 2 Sep. 2014 | P-M |
| 5 | 1300–1859 5 July 2014 | 2-V | 23 | 0600–0859 12 Sep. 2014 | P-M |
| 6 | 0000–0359 6 July 2014 | P-M | 24 | 0500–2059 23 Sep. 2014 | P-M |
| 7 | 0000–1059 9 July 2014 | P-M | 25 | 0500–1659 29 Sep. 2014 | P-M |
| 8 | 1400–2359 12 July 2014 | P-M | 26 | 0500–2359 12 Oct. 2014 | P-M |
| 9 | 0900–1859 16 July 2014 | 2-V | 27 | 1200–2259 12 Apr. 2015 | P-M |
| 10 | 0300–0459 17 July 2014 | 2-V | 28 | 1000–1659 13 Apr. 2015 | P-M |
| 11 | 1200–2359 18 July 2014 | 2-V | 29 | 0700–1059 22 Aug. 2015 | P-M |
| 12 | 0500–0959 28 July 2014 | P-M | 30 | 0800–1459 16 Sep. 2015 | P-M |
| 13 | 0900–1459 1 Aug 2014 | P-M | 31 | 0000–1259 23 Sep. 2015 | P-M |
| 14 | 0000–2359 2 Aug 2014 | P-M | 32 | 0000–2359 30 Sep. 2015 | P-M |
| 15 | 1400–2259 14 Aug. 2014 | 2-V | 33 | 0000–0859 1 Oct. 2015 | P-M |
| 16 | 1600–1759 17 Aug. 2014 | 2-V | 34 | 0500–1259 6 Apr. 2016 | P-M |
| 17 | 0000–2159 18 Aug. 2014 | 2-V | 35 | 0000–0459 24 May 2016 | P-M |
| 18 | 0300–1559 19 Aug. 2014 | P-M | 36 | 1100–2359 27 May 2016 | P-M |

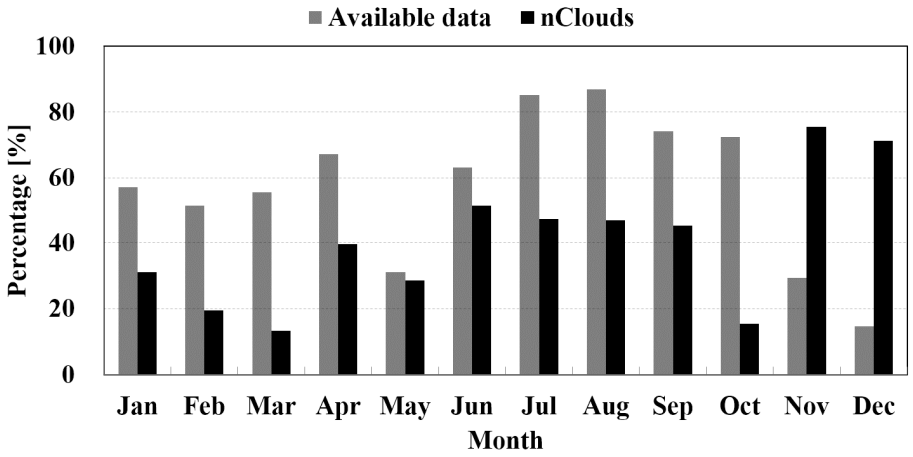


**Figure 2.** The monthly percentages of available reflectivity data (light bar) and cloud occurrences (dark bar) averaged from June 2014 to May 2016.

## 3. Methods

### *3.1. Quality Control and Reflectivity Calibration*

The non-meteorological echoes (e.g., insects and noises) were removed from the cloud radar data through using a simplistic quality control procedure. If the hardware burst power was less than 75 dB, the data were treated as noise and were removed. Data below a 300 m altitude were also removed by assuming ground clutter contamination. The data set was divided into two periods, namely the cold season from December to April, and the warm season from May to November, depending on the activity of insects and the height of the bright band. During the warm season, the height of the bright band was typically higher than 4 km and insect echoes were more frequent than in the cold season. The following thresholds were then applied for removing the non-meteorological echoes, in particular, radio interference and noise along the ray direction: $Z < -40$ dBZ or LDR > 0 dB for the cold season and $Z < -30$ dBZ below 4 km or LDR > −5 dB for the warm season. The additional

threshold (Z < 0 dBZ and LDR > −15 dB below 4 km) was applied to remove insect echoes during the "warm" season. Finally, the remaining non-meteorological echoes were removed through despeckling in the vertical direction (ray direction) by eliminating the cloud layer thinner than 150 m.

Figure 3 shows the time–height profiles of observed Z and LDR before (left panel) and after (right panel) applying quality control on 17 June 2014. Deep precipitation echoes (over 13 km) were observed from 0000 to 0500 UTC, followed by cloud echoes above 6 km and around 4 km and non-meteorological echoes below 3 km. A bright band appeared at 4–5 km with an LDR > −15 dBZ. The non-meteorological echoes below 3 km showed a larger LDR. Non-meteorological echoes were well removed by applying the quality control procedure (Figure 3b,d). However, some thin clouds and the edges of clouds were also eliminated by the continuity check. We applied this quality control to the reflectivity data of the entire case (from June 2014 to May 2016), and the quality controlled data were used for the further analysis of cloud properties.

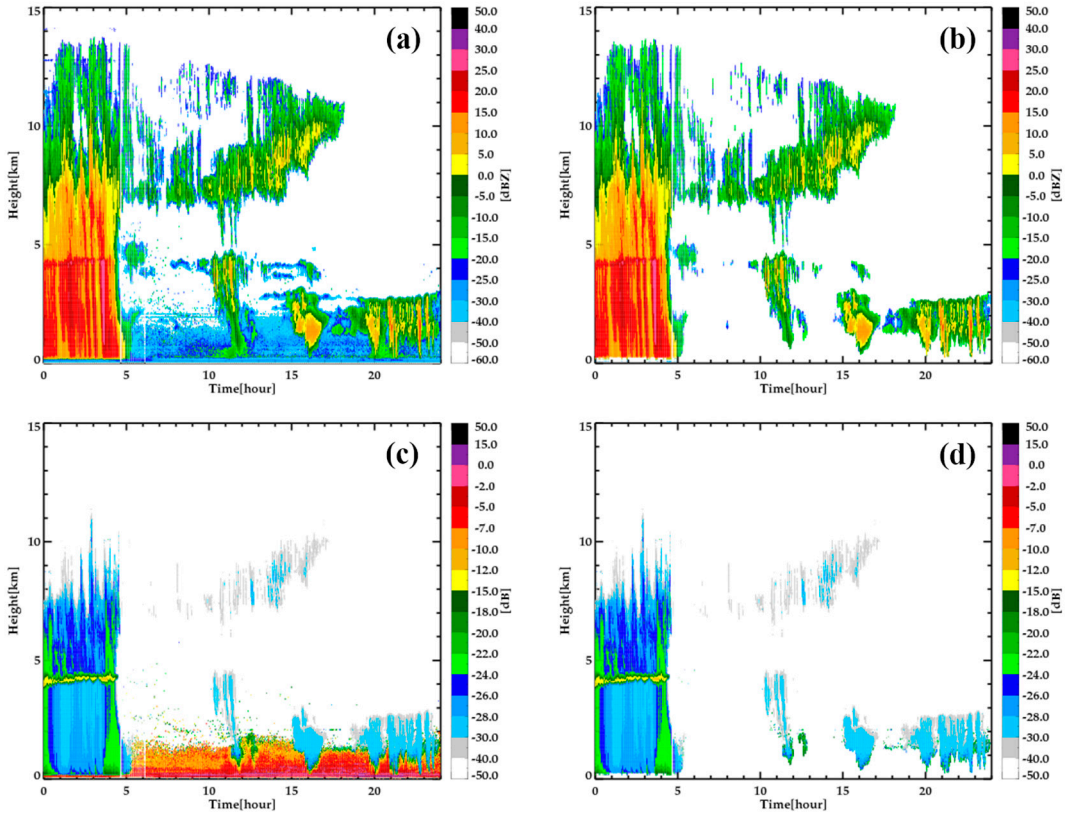


**Figure 3.** An example of (**a**,**b**) reflectivity and (**c**,**d**) linear depolarization ratio (LDR) before (left panel) and after (right panel) applying the quality control procedure.

The reflectivity of the cloud radar was absolutely calibrated by comparing it with the MRR and VertiX that were calibrated with the 2DVD and PARSIVEL. First, we examined the dependency of radar reflectivity in different wavelengths with the exponential DSD [34]. The reflectivity (Z) can be calculated from DSD using Equation (1) by assuming the spherical shape

$$Z = \int_{D_{min}}^{D_{max}} D^6 N(D) dD \quad (1)$$

where D is the particle diameter, N(D) is the number concentration of particles for a given D, and dD is the particle diameter bin or interval. However, the measured reflectivity depends on the particle shape and scattering characteristics. We applied the T-matrix simulation [35] for the three wavelengths (Ka for the cloud radar, K for the MRR, and X for the VertiX) with the condition shown in Table 3

and for the exponential DSDs [34]. The simulation results are shown in Figure 4. The $x$-axis is the reflectivity from Equation (1) with the exponential DSDs [34], and the different lines are from the T-matrix simulation for the wavelengths of Ka, K, and X-bands.

**Table 3.** Controlled conditions for the T-matrix simulation.

| Parameter | Value |
|---|---|
| Radar frequency | Ka-band (33.4 GHz)<br>K-band (24.0 GHz)<br>X-band (9.3 GHz) |
| Environment temperature | 10 °C |
| Radar elevation angle | 90° |
| Model hydrometeor type | Raindrop |
| Shape model of raindrop | Thurai et al. [36] |
| Canting angle of raindrops | Gaussian distribution with mean $\mu$ = 0° and standard deviation $\sigma$ = 10° |

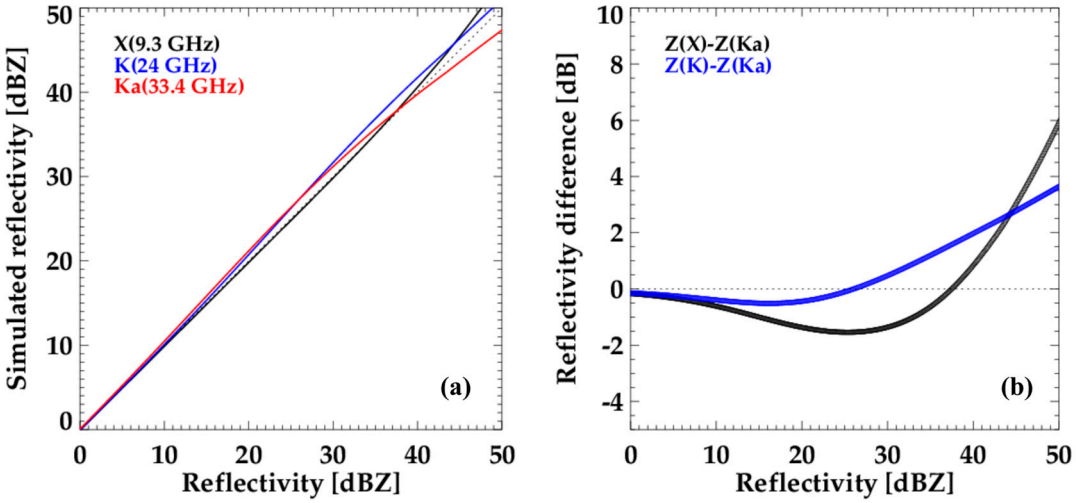


**Figure 4.** (**a**) Simulated reflectivities and (**b**) their differences in the three wavelengths, Ka (cloud radar), K (MRR), and X-band (VertiX) by assuming the Marshall–Palmer DSDs [35]. The $x$-axis is the reflectivity values from Equation (1), and the $y$-axis is derived from the scattering simulation with the condition shown in Table 3.

The reflectivity values from different wavelengths (X, K, and Ka-band) were almost identical when Z < 12 dBZ (Figure 4a). The difference in reflectivity values among different wavelengths became significant as Z > 20 dBZ due to the different scattering responses (Figure 4b). The Ka reflectivity was the largest when Z = 25 dBZ and the difference between the Ka and X-band was more than 1.5 dB. The difference between the K and Ka reflectivities was relatively smaller but became significant when Z > 33 dBZ due to the Mie effect. When comparing X–Ka and K–Ka reflectivities for calculating calibration values, we selected the reflectivity values smaller than 12 dBZ to avoid this difference among different wavelengths caused by the Mie effect. Thus, the calibration bias of the cloud radar was derived by comparing reflectivity smaller than 12 dBZ.

Second, the two vertical pointing radars (VertiX and MRR) were calibrated by comparing them with the ground-based disdrometers (2DVD and PARSIVEL). The correlation and mean bias of the reflectivities between the VertiX (MRR) and the 2DVD (PARSIVEL) were calculated at different altitudes. The altitude with the highest correlation was determined as the optimum altitude from which to derive the mean bias (calibration bias) for each rain event and was repeated for all the rain events listed in Table 2.

### *3.2. Classification of Cloud Types and Their Properties*

The cloud was first detected to classify cloud types using a 1 min reflectivity profile. An average of 10 bins was performed in the vertical direction to produce a 1 min reflectivity profile with 150 m spacing from 300 m above the ground level. The cloud was detected by the existence of at least three consecutive values in a 1 min reflectivity profile. Thus, the cloud depths shallower than 450 m were ignored. The base and top of the cloud were then determined by the lowest and highest height of the observed clouds.

Similar to the classification criteria of Kollias et al. [3], the cloud types were classified into rain (RC) and non-precipitating (high, middle, and lower) clouds with the existence of the observed reflectivity value at 300 m height. The non-precipitating clouds were categorized into high (HC), middle (MC), and low (LC) clouds based on the height of the cloud base, $H_b$, and top, $H_t$, (Table 4). If the cloud base height was 6 km or higher, it was classified as HC, if the cloud base height existed between 2 and 6 km, it was MC, LC had a $H_b$ between 300 m and 2 km. The RC was classified into the deep (RainDP) and shallow (RainSH) clouds according to their vertical extent using a threshold of 2 km. The classification of "shallow (RainSH) and deep (RainDP)" was applied only for precipitating clouds at the ground (measurable echoes at $H_b$ = 300 m in this study) and the vertical extent. Certainly, RainDP included precipitating clouds with multi-layer clouds. Middle and/or high clouds existed with the shallow layer of precipitating clouds, and they were not considered in the category of shallow (RainSH) in this study.

**Table 4.** Classification criteria of cloud types. The $H_b$ and $H_t$ indicate the height of the cloud base and the top.

| Cloud Type | | Criteria |
|---|---|---|
| High cloud (HC) | | $H_b \geq 6$ km |
| Middle cloud (MC) | | 2 km $\leq H_b <$ 6 km |
| Low cloud (LC) | | 300 m $< H_b <$ 2 km |
| Rain | Shallow (RainSH) | $H_t <$ 2 km<br>$H_b$ = 300 m |
| | Deep (RainDP) | $H_t \geq$ 2 km<br>$H_b$ = 300 m |

After classifying the different cloud types, the frequency of their occurrence and reflectivity were investigated. The monthly occurrence was defined as the ratio of the number of detected clouds to the total number of available observations (clouds in Figure 2). The seasonal frequency of cloud occurrence was calculated as the ratio of cloud data in each type to the total cloud data for a given season. Furthermore, the contoured frequency by altitude diagram (CFAD) was the frequency distribution of reflectivity according to the altitude and was used to analyze the cloud vertical structure [37]. The CFAD was obtained in an interval of 2 dBZ and the vertical distance of 150 m and was then normalized by the maximum frequency. The vertical mass flux, MF, was also calculated from Equation (2) [38]:

$$\mathrm{MF}\left[\mathrm{kgm^{-2}s^{-1}}\right] = \mathrm{M_c}\overline{\mathrm{V_c}} \tag{2}$$

where the mass content of clouds, $M_c$ is in kg m$^{-3}$, and the mass-weighted velocity $\overline{V_c}\left[\mathrm{m\,s^{-1}}\right]$ is derived from the radar Doppler velocity $\langle V_D \rangle$ with $\overline{V_c} = 0.85\langle V_D \rangle$. The mass content of clouds was calculated from Equation (3):

$$\mathrm{M_c} = 10^{-5}\mathrm{Z}^{0.5} \tag{3}$$

where Z is in mm$^6$ m$^{-3}$.

The vertical air velocity ($V_{air}$) was also calculated by the $V_t$–Z technique [39] to link with possible microphysical processes. Here, the $V_t$ was the reflectivity-weighted terminal fall velocity. This technique provided the best accuracy in the upper layer although the overall accuracy was not

the best. The $V_t$ was calculated using a power–law relationship between $V_t$ and Z [16,39,40] which was derived from an individual event:

$$V_t = aZ^b. \quad (4)$$

The a and b were derived as 0.88 (0.95) and 0.07 (0.16) for HC on 9 August 2015 (RainDP on 5 July 2014) case. Using the retrieved Equation (4) for each case, the $V_{air}$ can be calculated from Equation (5).

$$V_{air} = V_D - V_t \quad (5)$$

## 4. Results

### *4.1. Reflectivity Calibration*

We performed the reflectivity calibration for the 36 rain cases listed in Table 2. Figures 5 and 6 show the case of 2 July 2014 as an example. The time series of radar reflectivity obtained from the 2DVD, PARSIVEL, VertiX, MRR, and cloud radar showed higher Z in the VertiX and lower Z in the cloud radar when compared with either the 2DVD or PARSIVEL (Figure 5). Here, the measurement height of the MRR and cloud radar (VertiX) was 400 m (472 m) above ground level to avoid possible contamination by the ground clutter. The Z values from the cloud radar were rarely higher than 20 dBZ and flattened when Z(2DVD) > 25 dBZ due to strong attenuation by precipitation in the cloud radar. Thus, higher reflectivity should not be used when deriving the mean bias of the cloud radar. The correlation between the 2DVD and PARSIVEL was approximately 0.95, and the mean bias was 0.26 dB (not shown). Thus, either the 2DVD or PARSIVEL can be used as the ground truth.

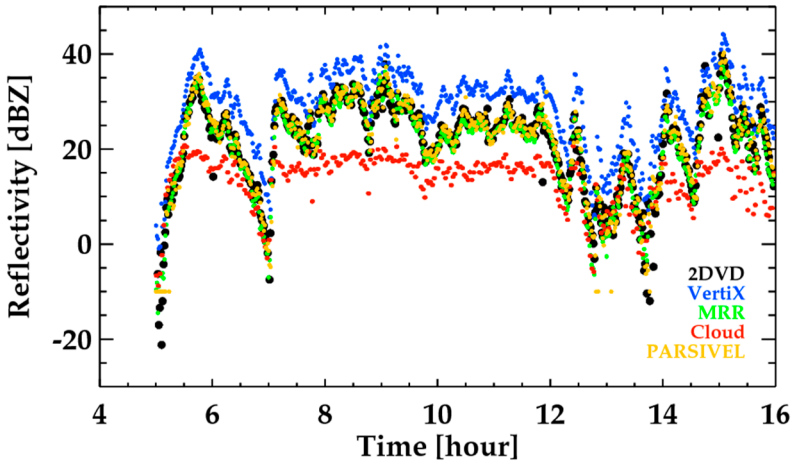


**Figure 5.** Time series of radar reflectivity from five instruments (black: 2DVD; yellow: PARSIVEL; blue: VertiX at 472 m height; green: MRR at 400 m height; red: cloud radar at 400 m height) from 0400 to 1600 UTC, 2 July 2014 (case 4 in Table 2).

The mean bias in 2DVD–VertiX and PARSIVEL–MRR was first calculated to derive the calibration bias of the VertiX and MRR (upper panels in Figure 6). These pairs were highly correlated in particular with moderate and heavy rain. The scatter increased in light rain. The mean bias of the VertiX (MRR) was approximately 7.7 dB (−0.7 dB). This bias was applied to the VertiX and MRR which were subsequently compared with the cloud radar. The scatter plot of the two pairs (cloud radar vs. VertiX, and cloud radar vs. MRR) showed a systematically lower Z from the cloud radar in the higher Z values. The scattering simulation showed a slightly higher Z in the cloud radar than the MRR (VertiX) when Z < 37 dBZ (25 dBZ) (Figure 4). Thus, the systematic discrepancy in Z with an increasing Z was not attributed to the scattering properties but the strong attenuation by precipitation. The Z difference due to the precipitation attenuation and scattering properties can be minimized by deriving the mean bias when Z < 12 dBZ. The mean bias of the cloud radar was about −0.5 dB (−0.2 dB) with the VertiX

(MRR). The different calibration paths (2DVD–VertiX–cloud radar and PARSIVEL–MRR–cloud radar) provided a similar calibration constant.

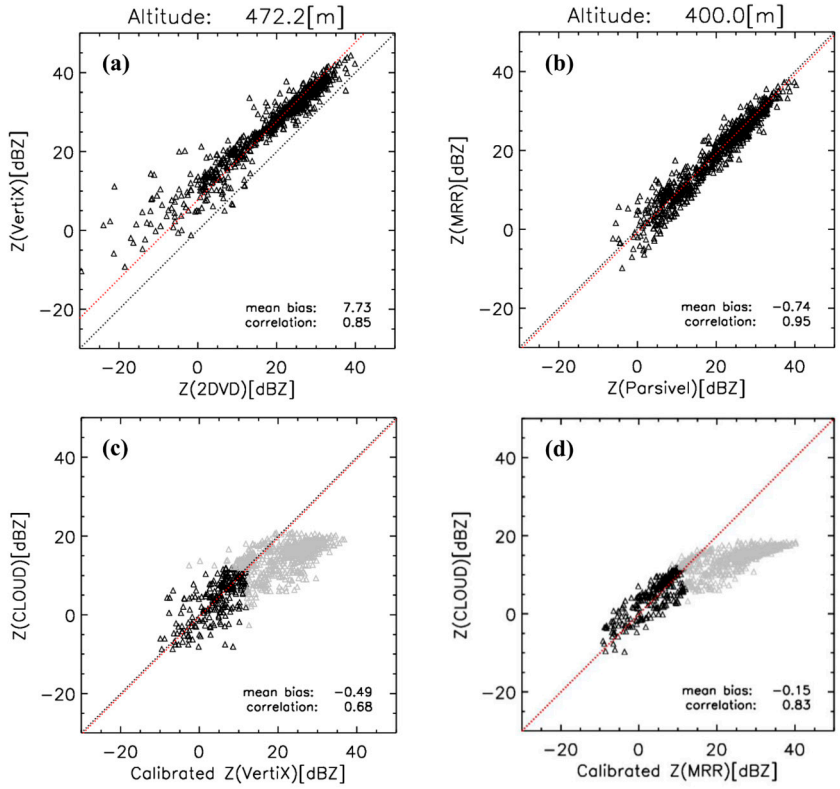


**Figure 6.** Scatter plots of radar reflectivity derived from 0400 to 1600 UTC, 2 July, 2014. (**a**) 2DVD vs. VertiX, (**b**) PARSIVEL vs. MRR, (**c**) calibrated VertiX vs. cloud radar, and (**d**) calibrated MRR vs. cloud radar. The mean bias is shown in the red line.

The same procedure was applied to the 36 rain cases from June 2014 to May 2016 and the calibration values (the opposite sign of the mean bias) of the MRR, VertiX, and cloud radar is shown in Figure 7. The calibration values of the MRR and VertiX were stable with time and their averages (standard deviation) were 0.9 dBZ (0.83 dB) for theMRR and −7.4 dBZ (0.48 dB) for the VertiX. The calibration values of the cloud radar were quite variable and their average value was about 2.2 dBZ with a standard deviation of 2.69 dB. The calibration values of the cloud radar with the VertiX and MRR were quite similar (red circle and black circles for eight events in the lower panel of Figure 7). When there was no derived calibration value, the calibration value derived from the nearest day was used.

### *4.2. Seasonal Variation of Cloud Properties*

The characteristics of the cloud occurrence were investigated in this section. The average annual cloud frequency was approximately 35.9%. The black bar in Figure 2 is the monthly cloud occurrence (normalized with the available data of the month) averaged from June 2014 to May 2016. The highest cloud occurrence, approximately 50%, showed in June when excluding the months with available data of lower than 30% (that is, May, November, and December were excluded due to the representativeness). The cloud was least frequent in March, less than 13%. Missing data existed over the short period of time (2 years). Therefore, the overall analysis did not represent reliable climatology. Furthermore, the quite significant data were missing due to unstable hardware conditions. Thus, given this, the overall seasonal variation of cloud properties in this section should be considered. Diurnal cycle and variation of vertical structures that were less affected by the missing data are shown in the next section.

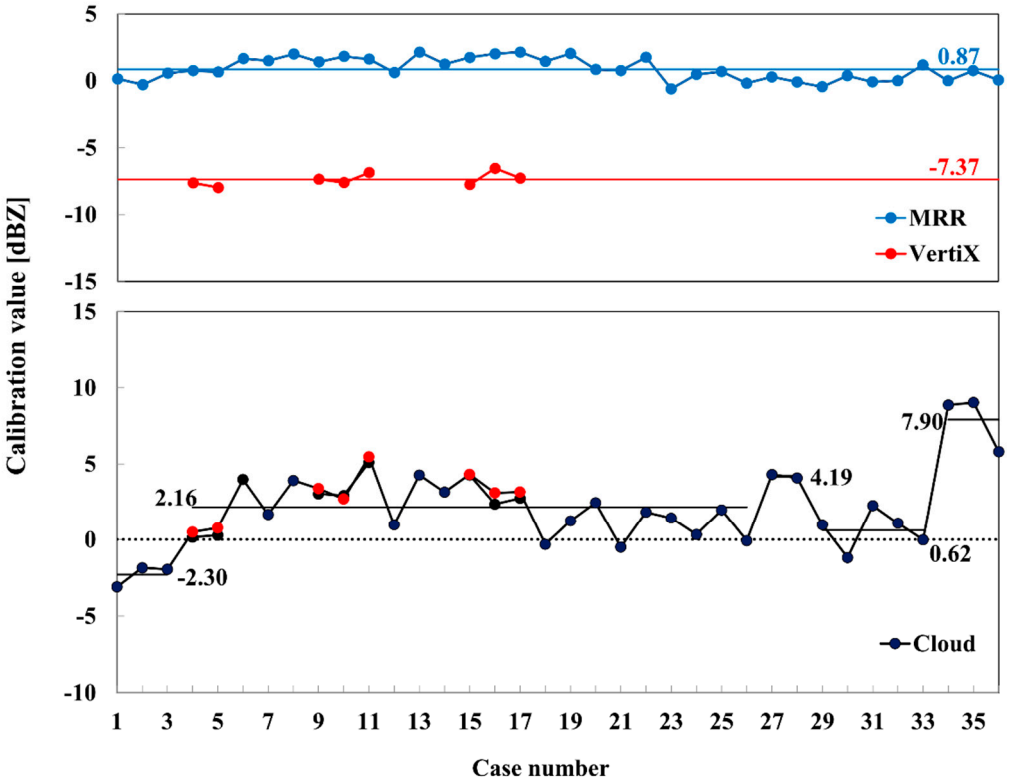


**Figure 7.** The calibration values of radar reflectivity from the three instruments during 36 rain events. Upper panel: MRR (blue) and VertiX (red); lower panel: cloud radar (black with MRR and red with VertiX).

The frequency of cloud occurrence was approximately 15.6% (43.5% of the yearly overall cloud occurrence) in summer, 8.6% (23.9%) in autumn, 5.2% (14.4%) in winter, and 6.5% (18.1%) in spring (Table 5). This result is similar to previous studies that analyzed the cloud frequency in East Asia. According to Cai et al. [41], the occurrence of clouds in summer and autumn was, in general, greater than in spring and winter over China, based on the cloud–aerosol lidar with orthogonal polarization (CALIOP) data. Lee et al. [23] also showed that the occurrence of clouds in summer accounts for the largest proportion of the yearly frequency in Seoul, Korea. Furthermore, the occurrence by cloud types showed the highest value in RainDP (11.8%; 32.9% of the yearly average cloud occurrence), followed by HC (9.3%; 26.0%), MC (7.4%; 20.6%), RainSH (4.4%; 12.0%), and LC (2.9; 8.2%). That is, approximately 45% of clouds were accompanied by precipitation, and the RainSH was approximately 27% of the precipitation. The previous analyses with the shorter period (2–3 months) showed a similar result that the LC containing precipitating clouds was the most frequent (Oh et al. [24] and Ye et al. [25]).

**Table 5.** Seasonal cloud occurrence by the cloud types. The average annual cloud frequency is approximately 35.9%.

| [%] | Spring | Summer | Autumn | Winter | Total |
|---|---|---|---|---|---|
| HC | 1.21 | 5.41 | 2.38 | 0.34 | 9.34 |
| MC | 1.27 | 2.83 | 1.88 | 1.42 | 7.41 |
| LC | 0.46 | 1.18 | 0.48 | 0.81 | 2.93 |
| RainSH | 1.11 | 0.93 | 0.84 | 1.51 | 4.40 |
| RainDP | 2.44 | 5.27 | 3.00 | 1.09 | 11.81 |
| Total | 6.51 | 15.62 | 8.59 | 5.18 | 35.90 |

In Figure 8, we examined the characteristics of the seasonal frequency of cloud occurrence by cloud type, and we normalized the frequency with the seasonal average occurrence in Table 5. The cloud

occurrence of HC and RainDP in summer was the largest (Figure 8 and Table 5). In particular, HC reached approximately 35% of the summer clouds and was as low as 6.6% in winter. The RainDP occurred in more than one third of the seasonal clouds except for winter. In particular, the RainDP and HC were approximately 68% in summer, which is similar to previous findings over China (Zhang et al. [42]). In the summer, the deep convection usually occurs due to the surface heating by the strong solar radiation [43–45]. Furthermore, the dynamic instability increased during the summer rainy seasons and precipitation frequently occurred. The clouds developing by deep convection and/or dynamic instability were possibly vertically extended and did not show any clear or no cloud regions in the vertical direction (this will be explored later). RainSH and LC most frequently occurred in winter (29% and 16%, respectively). Most of these shallow clouds are related to cloud development by the air–sea interaction during the cold air outbreak in winter in the Korea Peninsula [46–48]. When the Siberian high expands to the Korea Peninsula during the winter, oceans are relatively warmer than the cold air, leading to a shallow layer of conditionally unstable air with abundant moisture provided by the oceans. Convective but shallow clouds develop over the oceans and move to the land, leading to snow, which is the dominant process generating shallow clouds (RainSH and LC) in winter. The frequency of MC was higher in the cold season, namely 19.6%, 21.9%, and 27.4% in spring, autumn, and winter, respectively.

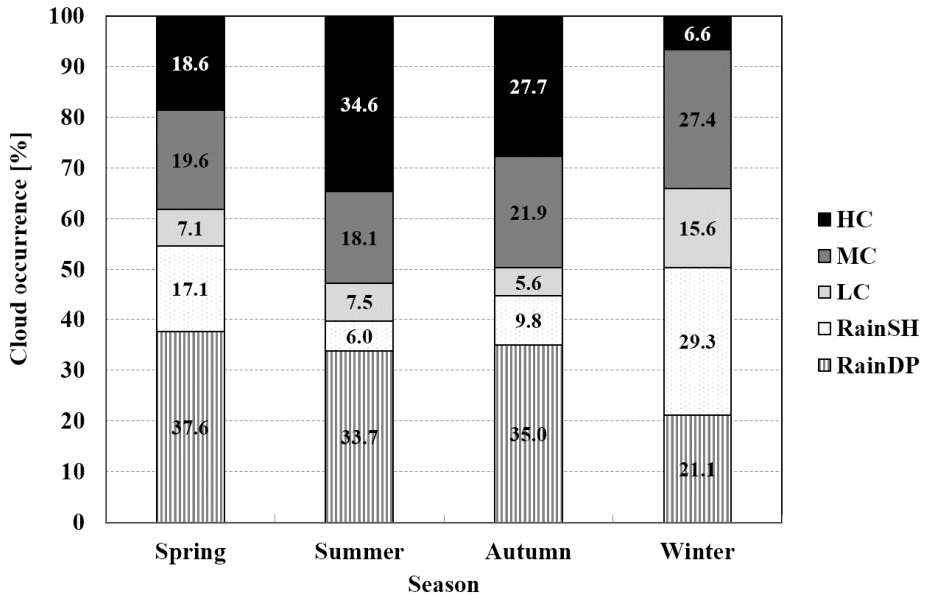


**Figure 8.** Seasonal frequency of cloud occurrence by cloud types. The frequency is normalized with the seasonal occurrence of clouds (6.5% in spring, 15.6% in summer, 8.6% in autumn, and 5.2% in winter), as shown in Table 5.

### *4.3. Diurnal Variation of Clouds*

The diurnal variation of cloud occurrence is shown for the cloud type and season (Figure 9). The HC had a diurnal variation with a high occurrence between 1800 and 0900 LST, and a lower frequency at 0900–1600 LST, except for winter. The diurnal variation of the altitude of the maximum frequency was significant in spring and autumn. In summer, the HC occurred in the wide range of the altitude. The MC in spring and winter had a similar pattern with a minimum occurrence during the day and a peak occurrence during the night. However, a maximum frequency appeared from 0300 to 1200 LST in autumn.

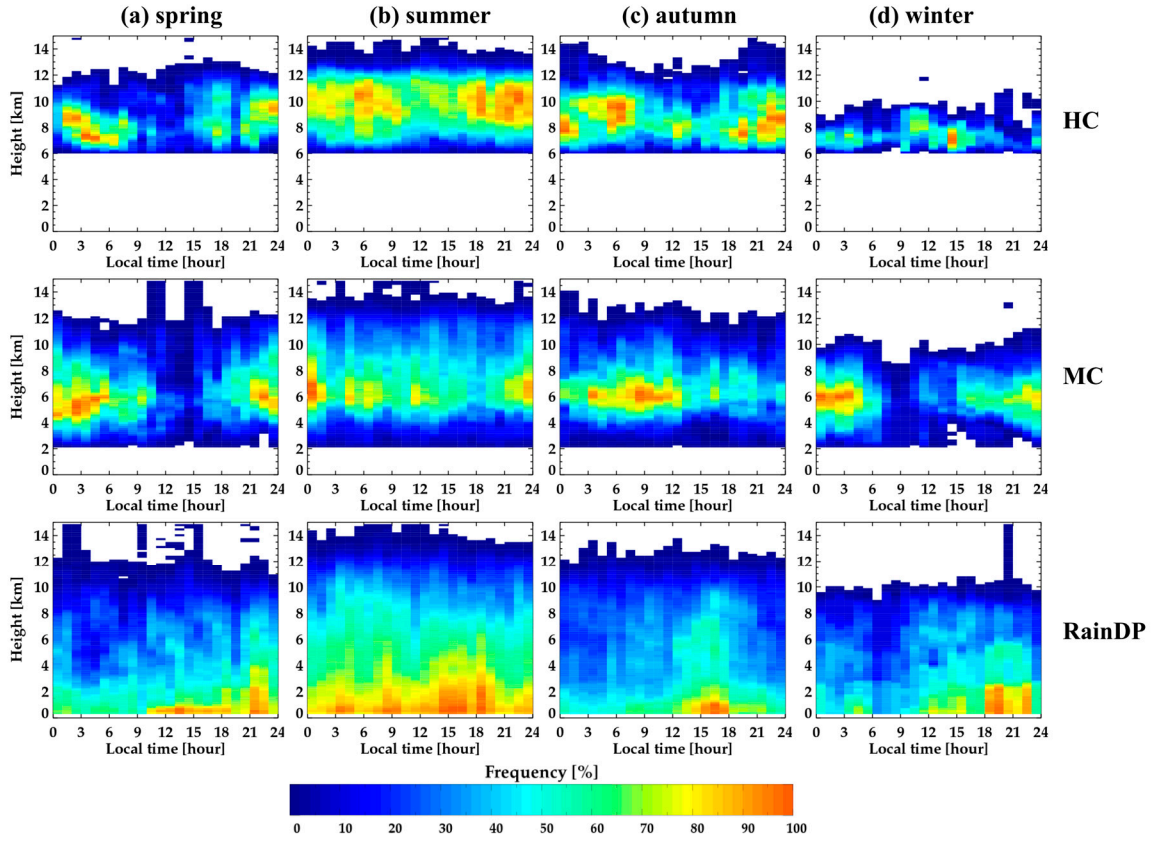


**Figure 9.** Diurnal variation of cloud occurrence for seasons and the different cloud types. (**a**) Spring, (**b**) summer, (**c**) autumn, and (**d**) winter. (Upper) HC, (middle) MC, and (lower) RainDP.

A clear single peak appeared in RainDP from 1200 to 1800 LST in autumn, however, this feature was inconsistent in other seasons. The high frequency appeared during the entire day in summer and two main peaks occurred from 0300 to 1000 LST and from 1400 to 2000 LST, which is consistent with the two peaks of the maximum frequency of precipitation in the early morning and late afternoon by Lim and Kwon [49]. Lee and Seo [50] also showed similar results that the diurnal and semidiurnal cycle peaks appear in the morning (0300–0900 LST) and the late afternoon (1600–2000 LST), respectively, in summer and winter over Korea. This maximum precipitation in the late afternoon is explained by ground heating by solar radiation and subsequently increased instability in the atmosphere. However, the frequent precipitation in the morning is related to the instability associated with radiative cooling in the upper atmosphere and complex processes of precipitation [50]. The weak diurnal variation in LC and RainSH was present (not shown).

### *4.4. Characteristics of Vertical Profiles*

Figure 10 shows the vertical profiles of the averaged reflectivity for the four seasons. The summer clouds had the highest reflectivity and the winter clouds had the lowest reflectivity at all heights. In summer and autumn, the average reflectivity increased sharply at approximately 4.5 km, indicating that a bright band was observed near this altitude. The bright band appeared near 2 km in winter. However, the bright bands were unclear in spring. There was no significant change of reflectivity with heights below 4 km in summer, but a significant decrease in reflectivity was noticeable below 1.5 km in spring and autumn.

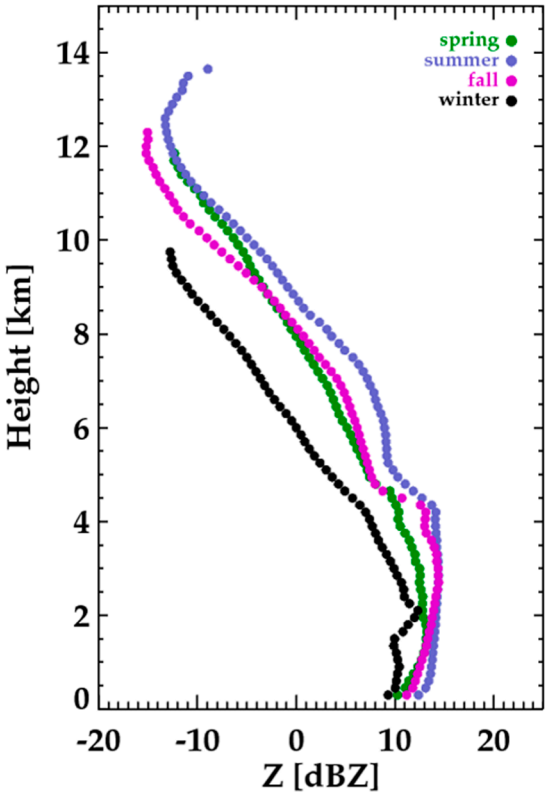


**Figure 10.** Vertical profiles of averaged reflectivity (Z) with seasons.

The slope of the average reflectivity can be related to the growth of cloud particles. The rapid increase in reflectivity above 7 km (roughly −15 °C with an assumption of pseudo-adiabatic lapse rate from the melting layer) in summer and autumn indicated the significant growth of ice particles. A smaller gradient of reflectivity appeared between 5 and 7 km, specifically in summer, indicating a rapid growth above 7 km (roughly −15 °C layer) and a relatively slower growth below 7 km. Further thorough studies are expected to understand this change in the growth rate related to the microphysical processes. However, this dramatic change of growth rate was less prominent in spring and winter; there was almost no change in the slope at 7 km in spring and a slight change at 4 km in winter.

The vertical structure of clouds was examined as CFADs of reflectivity and Doppler velocity for each season (Figure 11). The thickness of clouds was the largest in summer (approximately 14 km, Figure 11b), and the clouds were the thinnest in winter (Figure 11d). Furthermore, clouds occurred most frequently in summer and least in winter. The peak of frequency appeared at the two heights (the HC and LC region) for all seasons with a lower frequency in MC. The upper peak shifted to the lower layers from warm to cold seasons. The two modes (precipitation mode in $Z > 0$ dBZ and cloud mode in $Z < -10$ dBZ) were evident except for in summer. The cloud mode was dominant in spring and winter, while the precipitation mode was dominant in summer. The precipitation mode was linked with clouds in MC and HC, showing the downward increase in reflectivity in this dominant precipitation mode. This increase was the largest in the layer of 8–12 km in summer and was linked with the gradual increase (toward larger negative values) in Doppler velocity. A similar trend occurred in the different seasons to a smaller degree (the least increase in spring). Furthermore, the Doppler velocity became almost constant in the layer of 6–8 km in summer. This constant Doppler velocity with increasing reflectivity indicated the existence of a significant updraft in this layer. A similar but less prominent signature was shown in the Doppler velocity in autumn. The dramatic increase in Doppler velocity (toward negative values) was shown in the height of 3 to 5 km for spring, summer, and autumn, indicating the existence of a melting layer. The melting layer was the highest in summer and less prominent in winter, with some signature below 2.5 km.

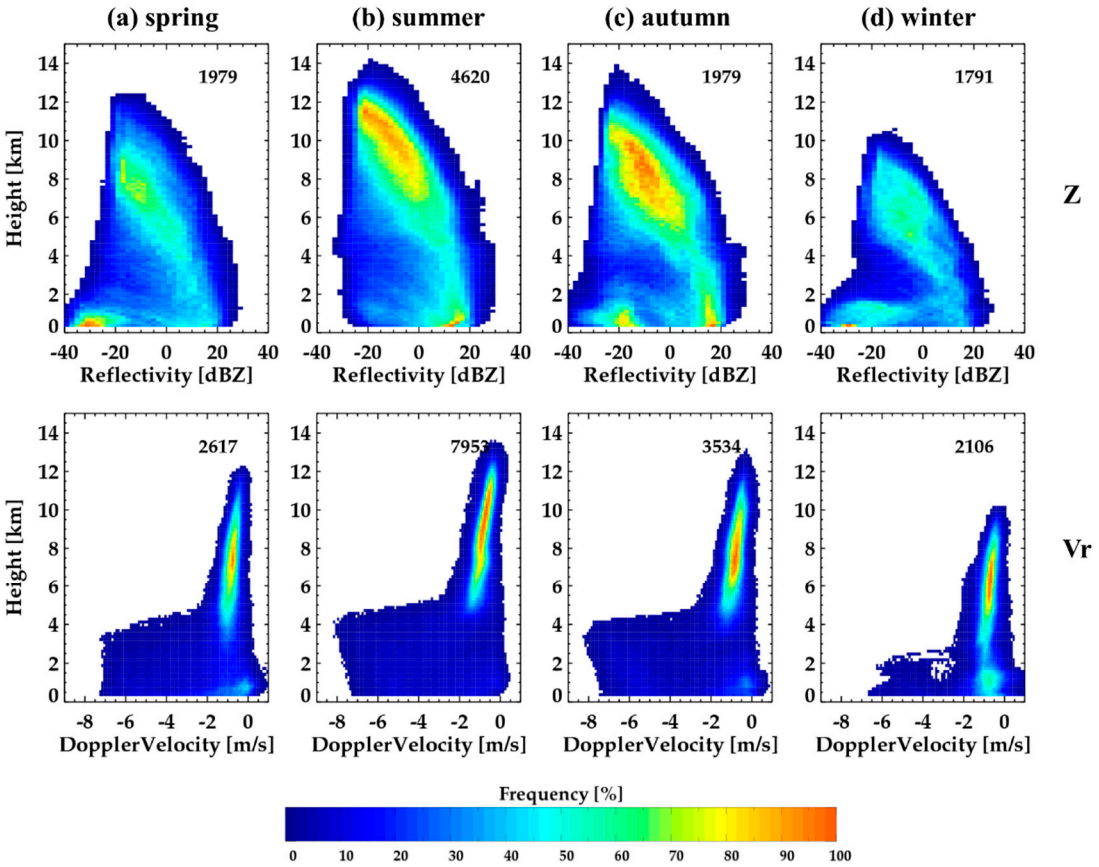


**Figure 11.** Contoured frequency by altitude diagrams (CFADs) of (upper) reflectivity and (lower) Doppler radial velocity for all types of clouds with seasons. (**a**) Spring, (**b**) summer, (**c**) autumn, and (**d**) winter. The number in each figure represents the maximum occurrence of clouds in the category of 2 dBZ reflectivity (0.1 m $s^{-1}$ velocity) and 150 m vertical resolution and is used to derive the percentile (color scale).

Seasonal CFADs were analyzed according to cloud types, HC, MC, and LC (Figures 12 and 13). The seasonal variation of the HC was prominent with the highest height in summer (10–12 km) and the lowest in winter (6–8 km). The dramatic growth appeared in the layer of 8–12 km in summer and of 9–10 km in autumn and was linked with the rapid increase in Doppler velocity in this layer (upper panels in Figure 13). Furthermore, this layer matched the maximum increase in the mass flux (upper panels in Figure 14). The largest mass flux was shown in summer. To further investigate the possible growth processes, we selected a HC case in the summer (9 August, 2015) and derived the vertical air velocity. A similar dramatic growth was shown in the CFAD of reflectivity (Figure 15). Both reflectivity and Doppler velocity rapidly increased with decreasing heights. However, the terminal fall velocity did not change (almost constant) with heights. A significant upward motion was shown throughout the HC regions, in particular above 9 km altitude. The updraft reached up to 0.9 m $s^{-1}$. This strong updraft led to the rapid growth of ice crystals by the depositional process and possibly the riming process in this layer during summer.

No significant increase in Doppler velocity and small mass flux was shown in winter. The reflectivity values were also smaller in winter. Furthermore, the CFAD of Doppler velocity was narrower in the upper layer and slowly broadened with decreasing heights, indicating the broadening of snow particles with different velocities, likely different mass and size of particles.

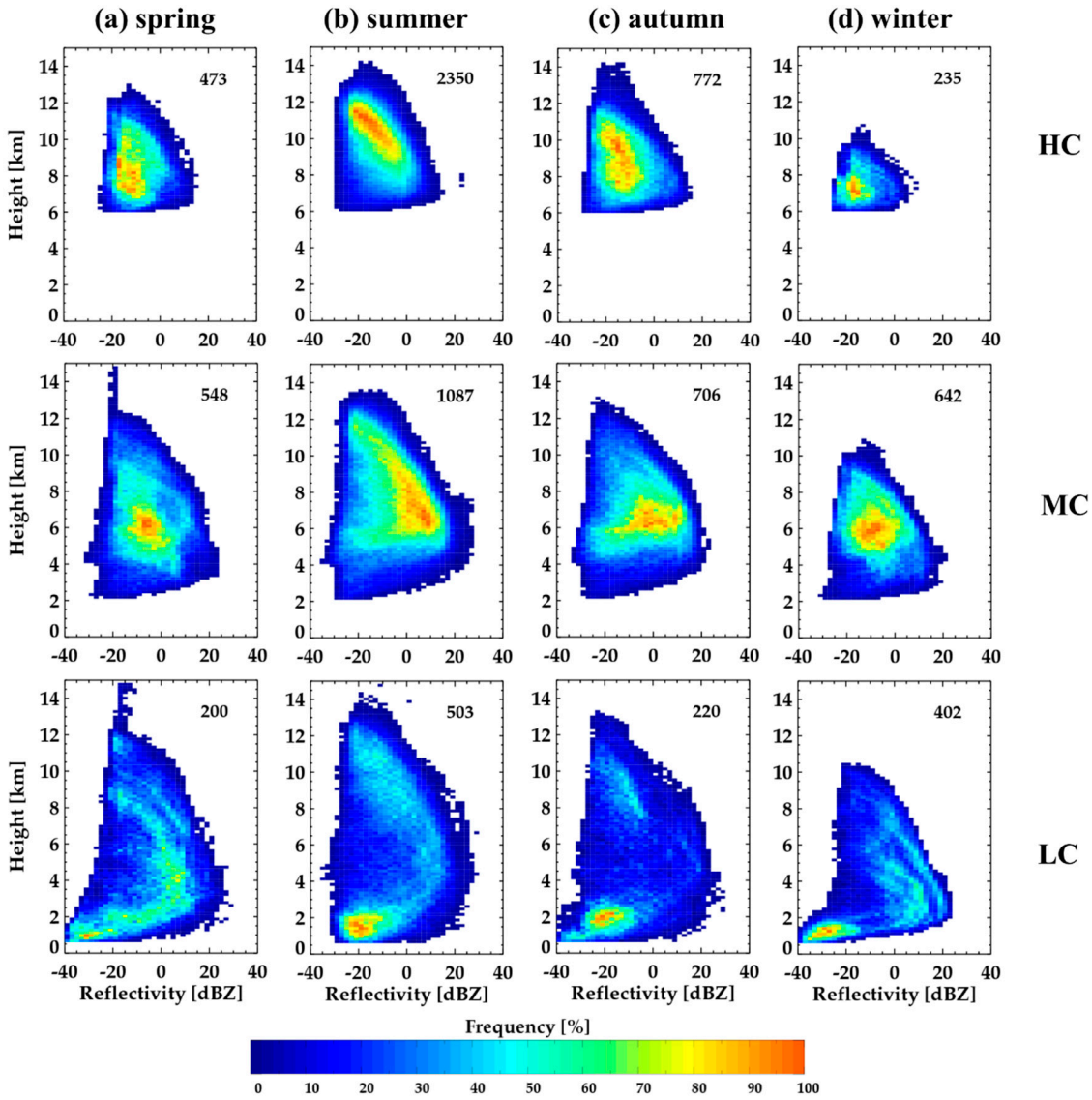


**Figure 12.** Seasonal CFADs of reflectivity for the different cloud types: (upper) HC, (middle) MC, and (lower) LC. (**a**) Spring, (**b**) summer, (**c**) autumn, and (**d**) winter.

Unlike HC, the height of the maximum reflectivity frequency appeared at similar heights (5–7 km) in MC, but the difference in reflectivity still existed with the largest value in summer and the smallest in winter (second row in Figure 12). Furthermore, the rapid growth appeared in the upper region of MC (HC region) in all seasons. This was also shown in the rapid increase in the Doppler velocity (see the second row in Figure 13) and mass flux (see the second row in Figure 14) in this upper region of MC. Different to HC, the reflectivity of MC rapidly decreased with heights in the lower layer (MC regions), which was linked with a near-constant Doppler velocity at heights between 4–7 km, except for in summer. The mass flux was nearly constant or decreased in this lower layer. Furthermore, the gradient of the Doppler velocity in summer was nearly constant in the layer of 6–8 km, although a rapid increase was shown in the lower and upper parts, indicating an updraft, as shown in the CFAD of the Doppler velocity in summer in Figure 13.

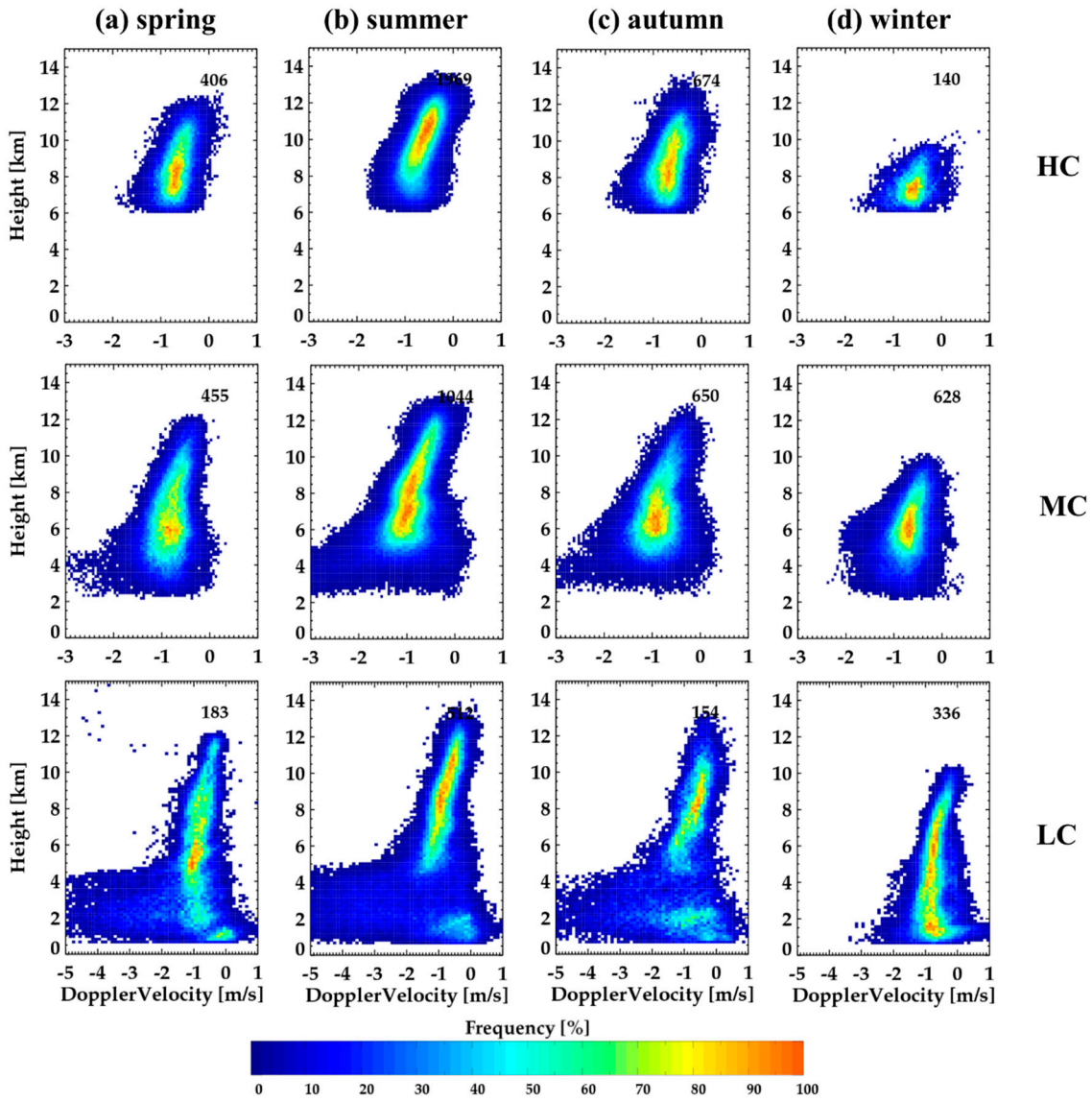


**Figure 13.** The same as in Figure 12 except for the CFADs of the Doppler radial velocity. (**a**) Spring, (**b**) summer, (**c**) autumn, and (**d**) winter.

LC showed a more dramatic change of reflectivity with heights. The rapid growth was shown in the upper layer, and a dramatic decrease appeared in the lower layer. This dramatic decrease was linked with the possible evaporation of precipitation particles, mostly raindrops, so that the cloud and precipitation particles did not reach the surface. The warm season showed two peaks of the frequency (upper and lower layers), while the cold season had a continuous frequency distribution. The peak of the frequency appeared in smaller Doppler velocity ranges (−1–0 $ms^{-1}$) due to dramatic evaporation in the lower layer. Similar to MC, updraft regions were present in the layer of 6–7 km in summer.

RainDP showed a rapid increase in reflectivity, in particular, in the upper HC layer during spring, summer, and autumn, while the winter RainDP had the largest gradient of reflectivity in the MC layer of 2–5 km (Figure 16), indicating the rapid growth of RainDP in the HC and MC regions. Unlike the CFAD in Figure 11, the frequency gradually increased with decreasing heights, with a dominant peak in the reflectivity range of 10–20 dBZ, indicating a continuous growth of clouds and precipitation particles in the MC regions instead of the strong evaporation shown in LC. The summer RainDP was the deepest and the winter RainDP showed the smallest depth. In particular, the summer RainDP had some clouds reaching 10 dBZ at 10 km. Furthermore, there was a signature of updraft (constant Doppler velocity) in the layer of 6–8 km with rapid increases in Doppler velocity above and below

the layer. These overall features in summer can be explained by the frequent vertical development of strong subtropical clouds due to synoptic forcing and vertical wind shear [51].

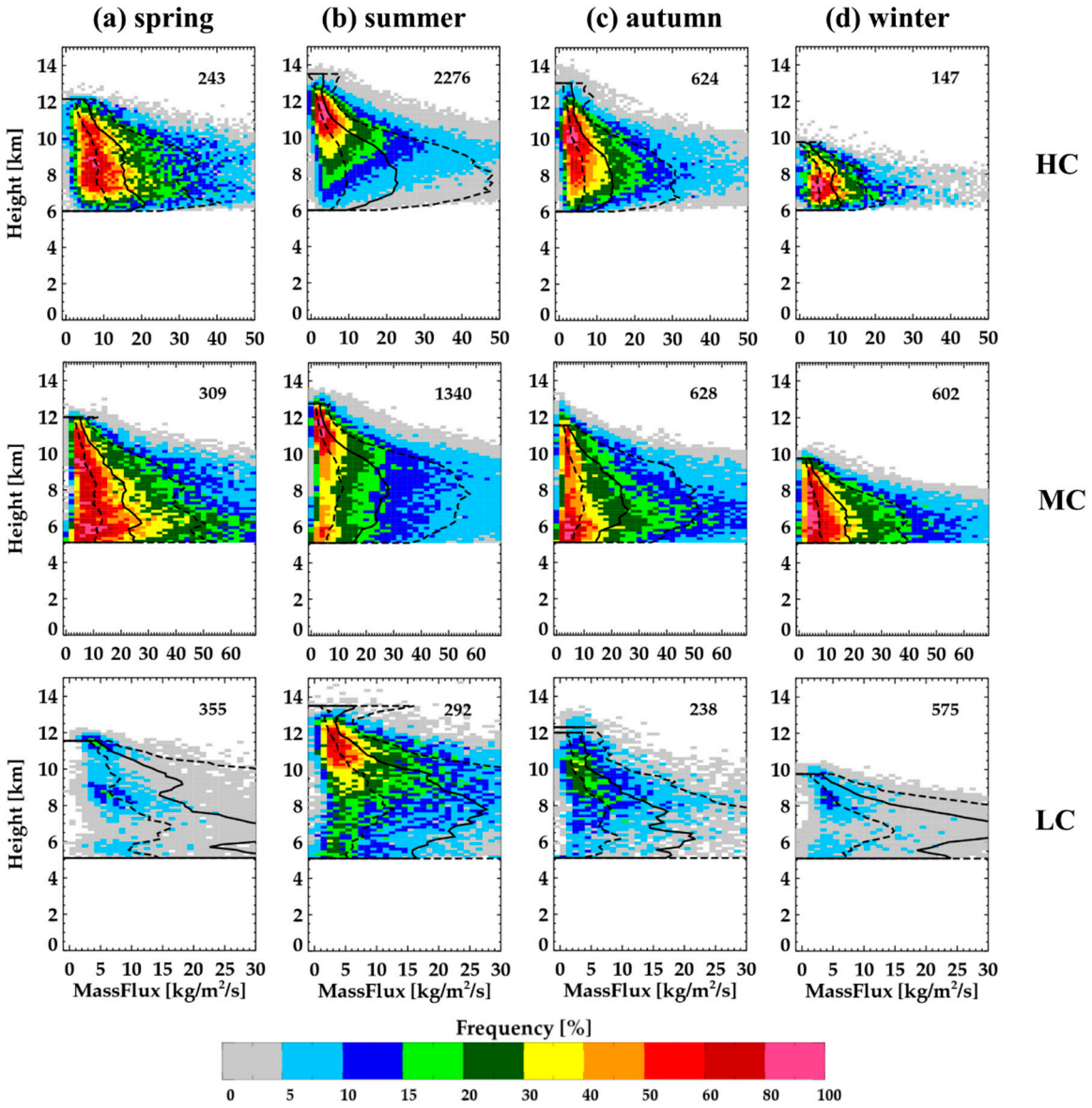


**Figure 14.** The same as in Figure 12 except for the CFADs of mass flux in the vertical direction. The median and quantiles (25% and 75%) are shown in the solid and dashed lines. (**a**) Spring, (**b**) summer, (**c**) autumn, and (**d**) winter.

The constant Doppler velocity was further examined for a RainDP case on 5 July, 2014. A similar analysis as in Figure 15 was applied for this case. The distinctive change of Z gradient was shown in the layers above and below 8 km. Similar to HC, the dramatic growth was linked with the rapid increase in the Doppler velocity, and a significant updraft that reached up to 1 m $s^{-1}$ (Figure 17). The Doppler velocity decreased in the layer below 8 km with decreasing heights and slightly increased in the layer below 7 km. The clear signature of updraft was shown in the layer of 6–8 km (see Figure 17d). The physical causes of this updraft region centered at 7 km (about −15 °C) are not certain and require further investigation.

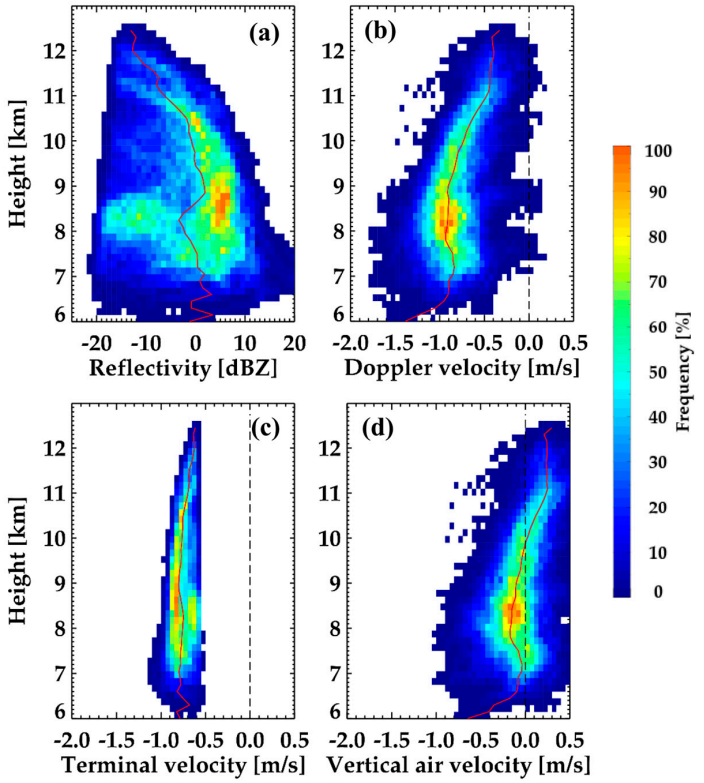


**Figure 15.** CFADs of (**a**) reflectivity, (**b**) Doppler velocity, (**c**) terminal velocity, and (**d**) vertical air velocity for a HC case on 9 August, 2015. The median is shown in the red line.

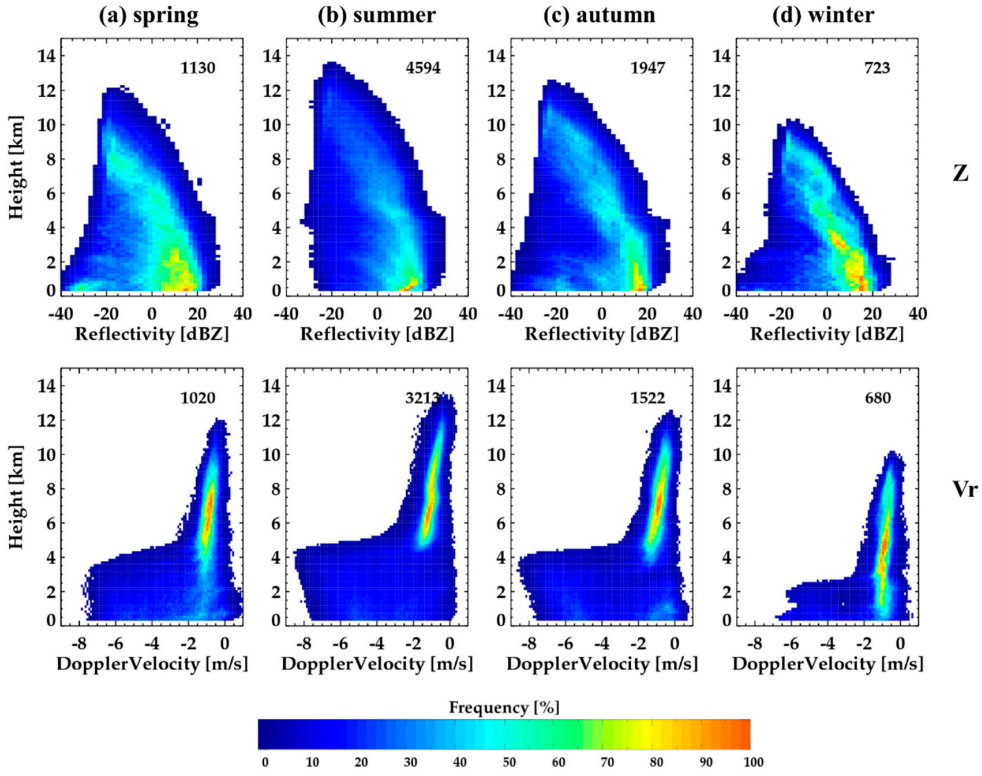


**Figure 16.** CFADs of (upper) reflectivity and (lower) Doppler radial velocity for RainDP with seasons. (**a**) Spring, (**b**) summer, (**c**) autumn, and (**d**) winter.

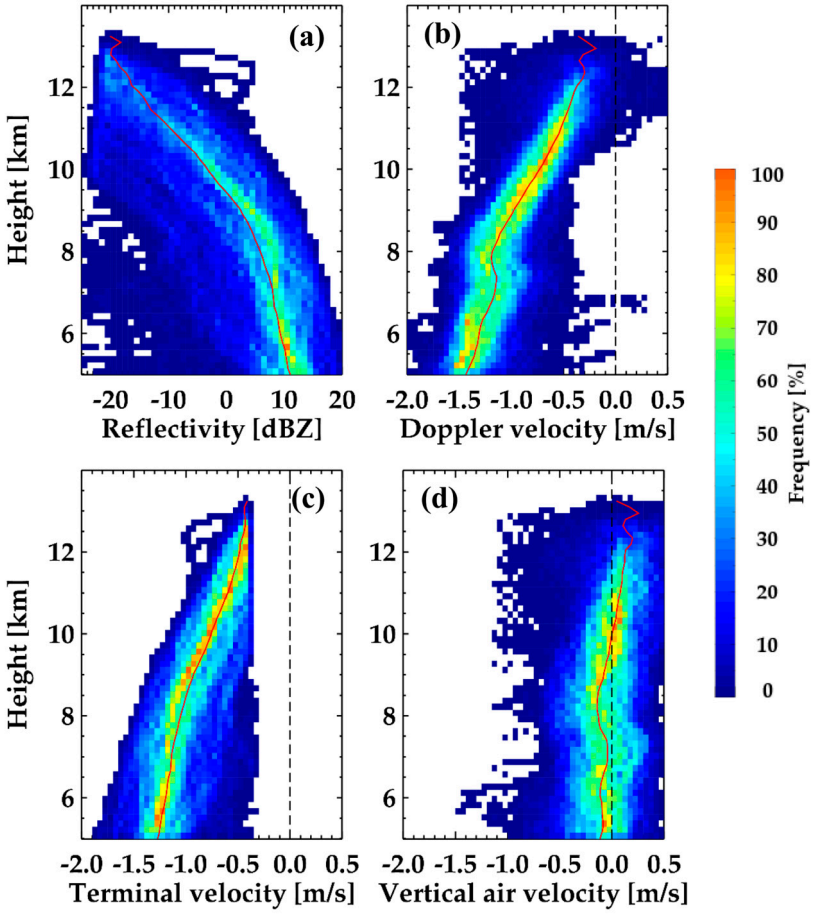


**Figure 17.** CFADs of (**a**) reflectivity, (**b**) Doppler velocity, (**c**) terminal velocity, and (**d**) vertical air velocity for a RainDP case on 5 July, 2014. The median is shown in the red line.

The RainDP could contain not only vertically developed single-layer precipitation clouds (top height ≥ 2 km) but also multi-layer clouds with shallow precipitation clouds below, and different layers of clouds above, due to the definition of the RainDP in this study. The RainDP was divided into the vertically continuous single-layer RainDP and multi-layer RainDP. The latter was identified by the no cloud area of at least 500 m layers in the vertical direction. Over 70% of RainDPs were the continuous single-layer RainDP (Figure 18). In particular, the single-layer RainDP was over 80% in summer and winter. This suggested that most RainDPs were single-layer precipitation clouds with strong vertical connections in the development of clouds and precipitation growth. The multi-layer RainDP was composed of RainSH below 2 km, and MC or mostly HC (lower panels in Figure 18).

The RainSH showed different characteristics with the seasons (Figure 19). Common rapid increases in reflectivity (Doppler velocity) were shown in summer, while the other seasons showed constant or decreasing reflectivity (Doppler velocity) due to evaporation. An updraft of larger than 1 m $s^{-1}$ occurred at a 1.5 km height in summer. In particular, the reflectivity gradient was about 20 dBZ $km^{-1}$ in the layer of 1.5 km (Z = −20 dBZ) to 0.5 km (Z = 0 dBZ), indicating that the growth of precipitation particles was the most efficient in summer. The updraft appeared in the lower layer in the different seasons and no systematic increases in the Doppler velocity were shown.

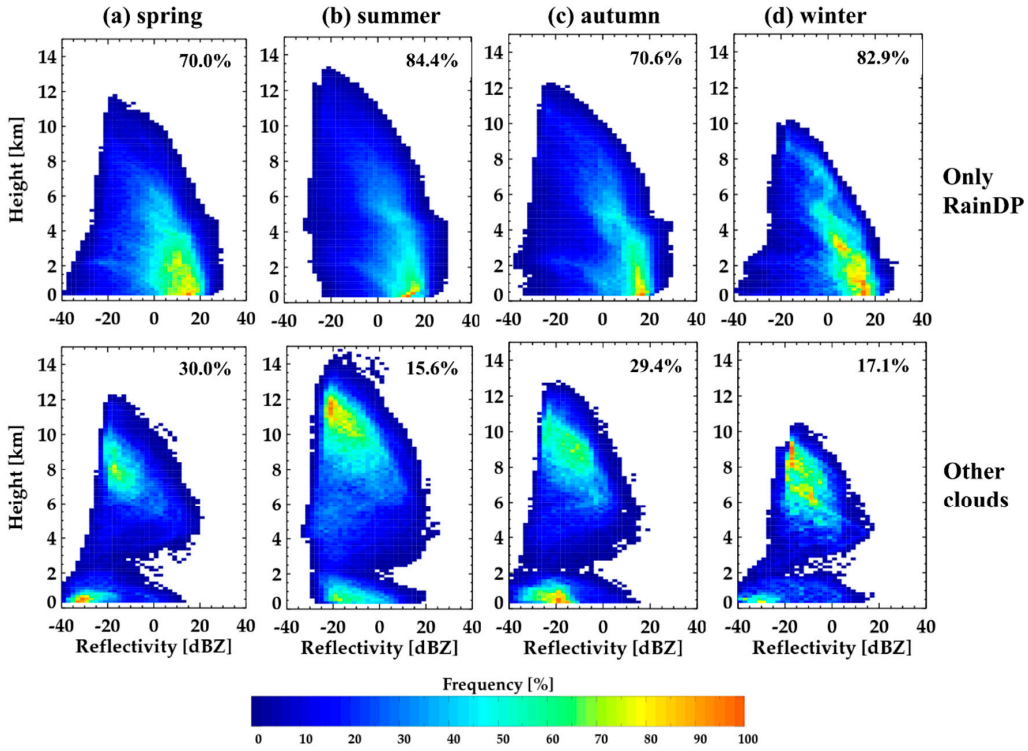


**Figure 18.** CFADs of reflectivity for (upper) vertically continuous RainDP and (lower) multi-layer RainDP with seasons. (**a**) Spring, (**b**) summer, (**c**) autumn, and (**d**) winter.

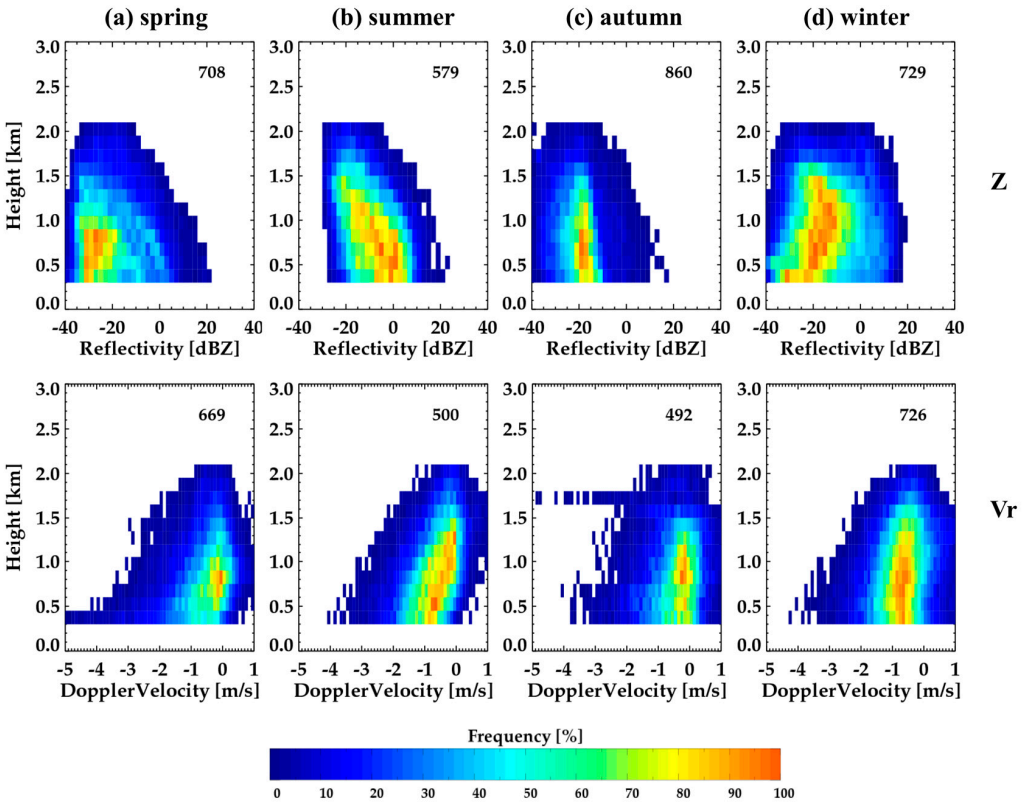


**Figure 19.** The same as in Figure 14, except for RainSH. (**a**) Spring, (**b**) summer, (**c**) autumn, and (**d**) winter.

## 5. Discussion

The updraft region in the 6–8 km layer (1–3 km above the melting layer) was prominent for MC, LC, and RainDP, particularly in the summer. This region coincides with constant Doppler velocity (its rapid increase above and below this layer) and the dramatic change of the vertical gradient of reflectivity. When we consider the pseudo-adiabatic lapse rate, the temperature of this region is approximately −20 to −7 °C. One possible cause of this updraft could be because of the dynamical instability such as strong wind shear or thermal instability. However, it is uncertain why these instabilities occur in the same layer. On the other hand, the melting could induce significant mesoscale circulation that could happen in the same height from the melting layer. Further thorough research will create a better understanding of this systematic updraft.

Recently, comprehensive studies on the retrieval of vertical air velocity in the vertically pointing radars have been explored [16,39,40,52]. Several methods were evaluated and their accuracies are documented. The growth rate and corresponding microphysical processes highly correlate with the vertical air motion. Furthermore, the high-resolution rawinsonde, ceilometer, and radiometer observation can further provide information on the liquid water path, environment air, and cloud base. Thus, further investigation of the microphysical processes is desired regarding the derived vertical air motion and other instrumentations.

This research is limited to the cloud data of only two years, and the cloud radar was somewhat unstable during the observation period. This study intends to provide a baseline for understanding cloud statistics and vertical structures and related microphysical processes. Further comprehensive studies are recommended with a long-term data set.

## 6. Conclusions

A ground-based cloud radar can be used to analyze cloud properties and the vertical distribution of clouds and help to understand the processes in cloud formation and development. In this study, we analyzed the occurrence and vertical structures of clouds for two years using cloud measurements from the Ka-band cloud radar at the Boseong site. The reflectivity of the cloud radar was first calibrated using two vertically pointing radars (VertiX and MRR) and two disdrometers (2DVD and PARSIVEL). The VertiX and MRR were compared with reflectivity derived from disdrometric measurements and the cloud radar reflectivity was subsequently compared with the calibrated reflectivity from the VertiX and MRR by considering the scattering effect and attenuation by precipitation. The non-meteorological echoes (insects, noise, etc.) were removed from the calibrated reflectivity of the cloud radar using the different thresholds of Z and LDR in warm and cold seasons and despeckling in the radial direction. The clouds are classified into the five types of precipitating (RainDP and RainSH) and non-precipitating clouds (HC, MC, and LC) by following the criteria of Kollias et al. [3]. We investigated the cloud occurrence and vertical structure of reflectivity, the Doppler velocity, and mass flux and their linkage with dominant microphysical processes for the five cloud types.

The average frequency of cloud occurrence was 35.9% over the observation period with the maximum frequency of 50% in June. The RainDP occurred most frequently (11.8%), followed by HC (9.3%), MC (7.4%), RainSH (4.4%), and LC (2.9%). The precipitating clouds (RainDP and RainSH) were almost 45% of the cloud occurrence. In particular, the HC and RainDP were frequently observed in summer and autumn due to strong surface heating and dynamic instability. However, RainSH, LC, and MC were dominant in the winter season. In particular, RainSH and LC were approximately 45% of the winter clouds and mostly due to cloud development by the air–sea interaction during the cold air outbreak.

We also examined the growth of cloud particles using the slope of the average reflectivity. The vertical gradient of reflectivity (with decreasing heights) above 7 km (about −15 °C layer) was larger and becomes smaller at 5–7 km, indicating that falling ice crystals grew faster above 7 km. Furthermore, this implies different growth modes or microphysical processes in the layer below and above 7 km. This change of vertical gradient was less significant in winter and spring.

The CFADs of reflectivity showed that the summer clouds are the thickest, and winter clouds are the thinnest. The peak of frequency appeared in the two heights (the HC and LC regions) with a low frequency in the MC region. Furthermore, the precipitation and cloud modes were shown in the LC region except for summer. The precipitation mode had a vertical linkage with MC and HC and showed a downward increase in reflectivity and Doppler radial velocity. However, the cloud mode was discontinuous with a lower frequency at the 2–4 km heights. A significant updraft dominantly exists in summer in the layer of 6–8 km (about 2–2.5 km above the melting layer).

The HC had a prominent seasonal variation with the highest height in summer and the lowest in winter. The rapid increase in reflectivity, the Doppler radial velocity, and mass flux in the layer above 7 km in the warm seasons (summer and autumn) indicated the possible growth of ice crystals by the riming processes in addition to depositional growth. A similar feature appeared in the autumn to a lesser extent. In contrast with HC, the peak frequency height of MC appeared in a similar height for all seasons with significant evaporation below this height. The Doppler velocity of MC rapidly increased in the layer above 8 km due to rapid growth, while it remained nearly constant below 8 km except for in summer. The mass flux was almost constant or decreased in this lower layer. The similar rapid growth in the upper layer and evaporation in the lower layer appeared in LC with a dramatic increase and reduction in reflectivity with decreasing heights. The evaporation was also supported by the frequency peak in the smaller Doppler velocity range (−1–0 m $s^{-1}$) near the ground. However, summer and autumn showed the two peaks in the upper and lower layers with a lower frequency in the MC region.

RainDP showed the continuous growth of precipitation particles in the entire layer, in particular in the upper HC and MC regions. The frequency of the precipitation mode increased toward the ground. RainSH showed the rapid increases in reflectivity and Doppler velocity in summer only. The precipitation growth was extremely efficient with the reflectivity gradient of about 20 dBZ $km^{-1}$. The updraft larger than 1 m $s^{-1}$ is present for all seasons and is stronger than that in the MC or HC regions.

**Author Contributions:** This work was made possible by significant contribution from all authors. Conceptualization, G.L. and B.-Y.Y.; methodology, B.-Y.Y., E.J., S.S., and G.L.; software, B.-Y.Y.; validation, B.-Y.Y. and G.L.; formal analysis, B.-Y.Y. and G.L.; investigation, B.-Y.Y. and G.L.; writing—original draft preparation, B.-Y.Y.; writing—review and editing, G.L., S.S., and E.J.; visualization, B.-Y.Y.; supervision, G.L.; funding acquisition, S.S. and G.L. All authors have read and agreed to the published version of the manuscript.

**Funding:** The data used in this work were provided by the Korea Meteorological Administration Research and Development Program "Enhancement of Convergence Technology of Analysis and Forecast on Severe Weather" under Grant (KMA2018-00121) and this work was funded by the Korea Meteorological Administration Research and Development Program under Grant KMI2018-06810.

**Acknowledgments:** We would like to thank Su-Bin Oh and Jeong-Eun Lee of KMA for acquiring the cloud radar, PARSIVEL, and MRR data. We also greatly appreciate students and researchers in CARE, KNU for participating in summer experiment 2014–2016.

**Conflicts of Interest:** The authors declare no conflict of interest.

## Abbreviations

| | |
|---|---|
| 2DVD | 2-dimensional video disdrometer |
| CFAD | Contoured frequency by altitude diagram |
| HC | High cloud |
| LC | Low cloud |
| LDR | Linear depolarization ratio |
| MC | Middle cloud |
| MRR | Micro rain radar |
| PARSIVEL | Particle size and velocity |
| RainDP | Rain deep cloud |
| RainSH | Rain shallow cloud |

| | |
|---|---|
| $V_D$ | Doppler velocity |
| VertiX | Vertically pointing X-band radar |
| Z | Reflectivity |

## References


1. Clothiaux, E.E.; Ackerman, T.P.; Mace, G.G.; Moran, K.P.; Marchand, R.T.; Miller, M.A.; Martner, B.E. Objective Determination of Cloud Heights and Radar Reflectivities Using a Combination of Active Remote Sensors at the ARM CART Sites. *J. Appl. Meteorol.* **2000**, *39*, 645–665. [CrossRef]
2. Wagner, T.J.; Kleiss, J.M. Error characteristics of ceilometer-based observations of cloud amount. *J. Atmos. Ocean. Technol.* **2016**, *33*, 1557–1567. [CrossRef]
3. Kollias, P.; Tselioudis, G.; Albrecht, B.A. Cloud climatology at the Southern Great Plains and the layer structure, drizzle, and atmospheric modes of continental stratus. *J. Geophys. Res. Atmos.* **2007**, *112*, 1–15. [CrossRef]
4. Chandra, A.S.; Kollias, P.; Giangrande, S.E.; Klein, S.A. Long-term observations of the convective boundary layer using insect radar returns at the SGP ARM climate research facility. *J. Clim.* **2010**, *23*, 5699–5714. [CrossRef]
5. Wood, C.R.; O'Connor, E.J.; Hurley, R.A.; Reynolds, D.R.; Illingworth, A.J. Cloud-radar observations of insects in the UK convective boundary layer. *Meteor. Appl.* **2009**, *16*, 491–500. [CrossRef]
6. Lohmeier, S.P.; Sekelsky, S.M.; Firda, J.M.; Sadowy, G.A.; Mclntosh, R.E. Classification of particles in stratiform clouds using the 33 and 95 ghz polarimetric cloud Profiling Radar System (CPRS). *IEEE Trans. Geosci. Remote Sens.* **1997**, *35*, 256–270. [CrossRef]
7. Luke, E.P.; Kollias, P.; Johnson, K.L.; Clothiaux, E.E. A technique for the automatic detection of insect clutter in cloud radar returns. *J. Atmos. Ocean. Technol.* **2008**, *25*, 1498–1513. [CrossRef]
8. Martner, B.E.; Moran, K.P. Using cloud radar polarization measurements to evaluate stratus cloud and insect echoes. *J. Geophys. Res. Atmos.* **2001**, *106*, 4891–4897. [CrossRef]
9. Zheng, J.; Liu, L.; Chen, H.; Gou, Y.; Che, Y.; Xu, H.; Li, Q. Characteristics of Warm Clouds and Precipitation in South China during the Pre-Flood Season Using Datasets from a Cloud Radar, a Ceilometer, and a Disdrometer. *Remote Sens.* **2019**, *11*, 3045. [CrossRef]
10. Lee, G.W.; Zawadzki, I. Radar calibration by gage, disdrometer, and polarimetry: Theoretical limit caused by the variability of drop size distribution and application to fast scanning operational radar data. *J. Hydrol.* **2006**, *328*, 83–97. [CrossRef]
11. Gage, K.S.; Williams, C.R.; Johnston, P.E.; Ecklund, W.L.; Cifelli, R.; Tokay, A.; Carter, D.A. Doppler Radar Profilers as Calibration Tools for Scanning Radars. *J. Appl. Meteorol.* **2000**, *39*, 2209–2222. [CrossRef]
12. Görsdorf, U.; Lehmann, V.; Bauer-Pfundstein, M.; Peters, G.; Vavriv, D.; Vinogradov, V.; Volkov, V. A 35-GHz polarimetric doppler radar for long-term observations of cloud parameters-description of system and data processing. *J. Atmos. Ocean. Technol.* **2015**, *32*, 675–690. [CrossRef]
13. Tridon, F.; Battaglia, A.; Kollias, P.; Luke, E.; Williams, C.R. Signal Postprocessing and Reflectivity Calibration of the Atmospheric Radiation Measurement Program 915-MHz Wind Profilers. *J. Atmos. Ocean. Technol.* **2013**, *30*, 1038–1054. [CrossRef]
14. Dong, X.; Xi, B.; Crosby, K.; Long, C.N.; Stone, R.S.; Shupe, M.D. A 10 year climatology of Arctic cloud fraction and radiative forcing at Barrow, Alaska. *J. Geophys. Res. Atmos.* **2010**, *115*, 1–14. [CrossRef]
15. Lazarus, S.M.; Krueger, S.K.; Mace, M.M. A Cloud Climatology of the Southern Great Plains ARM CART. *J. Clim.* **2000**, *13*, 1762–1775. [CrossRef]
16. Kalesse, H.; Kollias, P. Climatology of High Cloud Dynamics Using Profiling ARM Doppler Radar Observations. *J. Clim.* **2013**, *26*, 6340–6359. [CrossRef]
17. Zhang, J.; Chen, H. Macrophysical properties of specific cloud types from radiosonde and surface active remote sensing measurements over the ARM Southern Great Plains site. *Atmos. Ocean. Sci. Lett.* **2017**, *2834*, 1–7. [CrossRef]
18. Lamer, K.; Kollias, P.; Nuijens, L. Observations of the variability of shallow trade wind cumulus cloudiness and mass flux. *J. Geophys. Res. Atmos.* **2015**, *120*, 6161–6178. [CrossRef]
19. Kim, M.; Hong, S. Seasonal Change of the Frequency Percentage of Cloud Occurrence According to Its Type, Height and Amount in Korea. *Asia-Pac. J. Atmos. Sci.* **1991**, *27*, 353–364, (In Korean with English abstract).

20. Yeh, S.-W.; Kim, K.; Shin, K. Relationship between cloud type, cloudiness, surface temperature, and precipitation. In *Proceedings of the Spring Meeting of the Korean Meteorological Society, Busan, South Korea, 24–25 April 1997*; Korean Meteorological Society: Seoul, Korea, 1997; pp. 155–159. (In Korean)
21. Song, H.J.; Sohn, B.J. Two heavy rainfall types over the Korean Peninsula in the humid East Asian summer environment: A satellite observation study. *Mon. Weather Rev.* **2015**, *143*, 363–382. [CrossRef]
22. Cho, Y.-H.; Kim, K.-H.; Ha, J.-C.; Lim, E. Occurrence of cloud base height using ceilometer in Boseong, Korea. In *Proceedings of the Autumn Meeting of the Korean Meteorological Society, Jeju, South Korea, 12–14 October 2015*; Korean Meteorological Society: Seoul, Korea, 2015; pp. 262–263. (In Korean)
23. Lee, S.; Hwang, S.O.; Kim, J.; Ahn, M.H. Characteristics of cloud occurrence using ceilometer measurements and its relationship to precipitation over Seoul. *Atmos. Res.* **2018**, *201*, 46–57. [CrossRef]
24. Oh, S.B.; Kim, Y.H.; Kim, K.H.; Cho, C.H.; Lim, E. Verification and correction of cloud base and top height retrievals from Ka-band cloud radar in Boseong, Korea. *Adv. Atmos. Sci.* **2016**, *33*, 73–84. [CrossRef]
25. Ye, B.-Y.; Lee, G.; Kwon, S.; Lee, H.-W.; Ha, J.-C.; Kim, Y.-H. Preliminary Analysis of Data Quality and Cloud Statistics from Ka-Band Cloud Radar. *Atmosphere* **2015**, *25*, 19–30, (In Korean with English abstract). [CrossRef]
26. Oh, S.; Won, H.Y.; Ha, J.; Chung, K. Comparison of Cloud Top Height Observed by a Ka-band Cloud Radar and COMS. *Atmosphere* **2014**, *24*, 39–48, (In Korean with English abstract). [CrossRef]
27. Korea Meteorological Administration (KMA). Analysis Report of Climate Change in Boseong-gun, Jeollanam-do. Seoul, South Korea, 2015; 11-1360000-001180-01, p. 62. Available online: http://www.climate.go.kr/home/cc_data/scenario_web_report/Jeonnam_Boseong.pdf (accessed on 10 July 2020). (In Korean).
28. Park, S.-G.; Lee, G. Calibration of radar reflectivity measurements from the KMA operational radar network. *Asia-Pac. J. Atmos. Sci.* **2020**, *46*, 243–259. [CrossRef]
29. Chang, W.-Y.; Lee, G.; Jou, B.J.-D.; Lee, W.-C.; Lin, P.-L.; Yu, C.-K. Uncertainty in Measured Raindrop Size Distributions from Four Types of Collocated Instruments. *Remote Sens.* **2020**, *12*, 1167. [CrossRef]
30. Lee, G.W.; Zawadzki, L. Variability of drop size distributions: Noise and noise filtering in disdrometric data. *J. Appl. Meteorol.* **2005**, *44*, 634–652. [CrossRef]
31. Tokay, A.; Bashor, P.G.; Wolff, K.R. Error Characteristics of Rainfall Measurements by Collocated Joss–Waldvogel Disdrometers. *J. Atmos. Ocean. Technol.* **2005**, *22*, 513–527. [CrossRef]
32. Thurai, M.; Gatlin, P.; Bringi, V.N.; Petersen, W.; Kennedy, P.; Notaroš, B.; Carey, L. Toward completing the raindrop size spectrum: Case studies involving 2D-video disdrometer, droplet spectrometer, and polarimetric radar measurements. *J. Appl. Meteorol. Clim.* **2017**, *56*, 877–896. [CrossRef]
33. Kruger, A.; Krajewski, W.F. Two-Dimensional Video Disdrometer: A Description. *J. Atmos. Ocean. Technol.* **2002**, *19*, 602–617. [CrossRef]
34. Marshall, J.S.; Palmer, W.M.K. The distribution of raindrops with size. *J. Meteor.* **1948**, *5*, 165–166. [CrossRef]
35. Mishchenko, M.I.; Travis, L.D.; Mackowski, D.W. T-matrix computations of light scattering by nonspherical particles: A review. *J. Quant. Spectrosc. Radiat. Transf.* **1996**, *55*, 535–575. [CrossRef]
36. Thurai, M.; Huang, G.J.; Bringi, V.N.; Randeu, W.L.; Chönhuber, M. Drop shapes, model comparisons, and calculations of polarimetric radar parameters in rain. *J. Atmos. Ocean. Technol.* **2007**, *24*, 1019–1032. [CrossRef]
37. Yuter, S.E.; Houze, R.A., Jr. Three-Dimensional Kinematic and Microphysical Evolution of Florida Cumulonimbus. Part II: Frequency Distributions of Vertical Velocity, Reflectivity, and Differential Reflectivity. *Mon. Weather Rev.* **1995**, *123*, 1941–1963. [CrossRef]
38. Zawadzki, I.; Szyrmer, W.; Bell, C.; Fabry, F. Modeling of the melting layer. Part III: The density effect. *J. Atmos. Sci.* **2005**, *62*, 3705–3723. [CrossRef]
39. Protat, A.; Williams, C.R. The Accuracy of Radar Estimates of Ice Terminal Fall Speed from Vertically Pointing Doppler Radar Measurements. *J. Appl. Meteor. Climatol.* **2011**, *50*, 2120–2138. [CrossRef]
40. Kalesse, H.; Kollias, P.; Szyrmer, W. On using the relationship between Doppler velocity and radar reflectivity to identify microphysical process in midlatitudinal ice clouds. *J. Geophys. Res. Atmos.* **2013**, *118*, 12168–12179. [CrossRef]
41. Cai, H.; Feng, X.; Chen, Q.; Sun, Y.; Wu, Z.; Tie, X. Spatial and Temporal Features of the Frequency of Cloud Occurrence over China Based on CALIOP. *Adv. Meteorol.* **2017**, *2017*. [CrossRef]

42. Zhang, Y.; Zhou, Q.; Lv, S.; Jia, S.; Tao, F.; Chen, D.; Guo, J. Elucidating cloud vertical structures based on three-year Ka-band cloud radar observations from Beijing, China. *Atmos. Res.* **2019**, *222*, 88–99. [CrossRef]
43. Hong, S.-Y.; Lee, J.-W. Assessment of the WRF model in reproducing a flash-flood heavy rainfall event over Korea. *Atmos. Res.* **2009**, *93*, 818–831. [CrossRef]
44. Jo, E.; Park, C.; Son, S.; Roh, J.-W.; Lee, G.-W.; Lee, Y.-H. Classification of Localized Heavy Rainfall Events in South Korea. *Asia-Pac. J. Atmos. Sci.* **2020**, *56*, 77–88. [CrossRef]
45. Lee, T.-Y.; Kim, Y.-H. Heavy Precipitation Systems over the Korean Peninsula and their Classification. *J. Korean Meteor. Soc.* **2007**, *43*, 367–396.
46. Byun, K.-Y.; Yang, J.; Lee, T.-Y. A Snow-Ratio Equation and Its Application to Numerical Snowfall Prediction. *Weather Forecast.* **2008**, *23*, 644–658. [CrossRef]
47. Cheong, S.-H.; Byun, K.-Y.; Lee, T.-Y. Classification of Snow over the Korean Peninsula Based on Developing Mechanism. *Atmosphere* **2006**, *16*, 33–48, (In Korean with English abstract).
48. Park, H.-H.; Lee, J.; Chang, E.-C.; Joh, M. High-Resolution Simulation of Snowfall over the Korean Eastern Coastal Region Using WRF Model: Sensitivity to Domain Nesting-Down Strategy. *Asia-Pac. J. Atmos. Sci.* **2019**, *55*, 493–506. [CrossRef]
49. Lim, G.-H.; Kwon, H.-J. Diurnal Variation of Precipitations over south Korea and its Implication. *J. Korean Meteor. Soc.* **1998**, *34*, 222–237.
50. Lee, G.-H.; Seo, K.-H. Analysis of Diurnal and Semidiurnal Cycles of Precipitation over South Korea. *Atmosphere* **2008**, *18*, 475–483, (In Korean with English abstract).
51. Seo, E.-K. Characteristics of Summer Rainfall over East Asia as Observed by TRMM PR. *J. Korean Earth Sci. Soc.* **2011**, *32*, 33–45. [CrossRef]
52. Shupe, M.D.; Comstock, J.M.; Turnuer, D.D.; Mace, G.G. Cloud Property Retrievals in the ARM Program. *Meteorol. Monogr.* **2016**, *57*, 19.1–19.20. [CrossRef]


© 2020 by the authors. Licensee MDPI, Basel, Switzerland. This article is an open access article distributed under the terms and conditions of the Creative Commons Attribution (CC BY) license (http://creativecommons.org/licenses/by/4.0/).